Annually-resolved propagation of CFCs and SF6 in the global ocean over eight decades

Laura Cimoli[1], Geoffrey Gebbie[2], Sarah G. Purkey[3], and William M Smethie[4]

[1]University of California, San Diego
[2]Woods Hole Oceanographic Institution
[3]Scripps Institution of Oceanography, UCSD
[4]Lamont-Doherty Earth Observatory of Columbia University

November 23, 2022

Abstract

Oceanic transient tracers, such as chlorofluorocarbons (CFCs) and sulfur-hexafluoride (SF6), trace the propagation of intermediate-to-abyssal water masses in the ocean interior. Their temporal and spatial sparsity, however, has limited their utility in quantifying the global ocean circulation and its decadal variability. The Time-Correction Method presented here is a new approach to leverage the available CFCs and SF6 observations to solve for the Green's functions describing the steady-state transport from the surface to the ocean interior. From the Green's functions, we reconstruct global tracer concentrations (and associated uncertainties) in the ocean interior at annual resolution (1940 to 2021). The spatial resolution includes 50 neutral density levels that span the water column along WOCE/GO-SHIP lines. The reconstructed tracer concentrations return a global view of CFCs and SF6 spreading into new regions of the interior ocean, such as the deep north-western Pacific. For example, they capture the southward spreading and equatorial recirculation of distinct NADW components, and the spreading of CFC-rich AABW out of the Southern Ocean and into the North Pacific, East Indian, and West Atlantic. The reconstructed tracer concentrations fit the data in most locations (˜75%), indicating that a steady-state circulation holds for the most part. Discrepancies between the reconstructed and observed concentrations offer insight into ventilation rate changes on decadal timescales. As an example, we infer decadal changes in Subantartic Mode Water (SAMW) and find an increase in SAMW ventilation from 1992 to 2014, highlighting the skill of the time-correction method in leveraging the sparse tracer observations.

Annually-resolved propagation of CFCs and SF_6 in the global ocean over eight decades

Laura Cimoli[1], Geoffrey Gebbie[2], Sarah G. Purkey[1], William M. Smethie[3]

[1]Scripps Institution of Oceanography, University of California, San Diego
[2]Woods Hole Oceanographic Institution, Woods Hole, Massachusetts
[3]Lamont-Doherty Earth Observatory, Columbia University

Key Points:

- New "time-correction" method permits an annually-resolved global view of CFCs and SF_6 over eight decades
- Steady-circulation solution is simultaneously consistent with atmospheric histories and 75% of the $\sim 10^6$ total CFC and SF_6 observations
- CFCs and SF_6, now detected in most of the global ocean, allow for a synopsis of the interior ocean age, ventilation time, and variability

Corresponding author: Laura Cimoli, lcimoli@ucsd.edu

Abstract

Oceanic transient tracers, such as chlorofluorocarbons (CFCs) and sulfur-hexafluoride (SF_6), trace the propagation of intermediate-to-abyssal water masses in the ocean interior. Their temporal and spatial sparsity, however, has limited their utility in quantifying the global ocean circulation and its decadal variability. The *Time-Correction Method* presented here is a new approach to leverage the available CFCs and SF_6 observations to solve for the Green's functions describing the steady-state transport from the surface to the ocean interior. From the Green's functions, we reconstruct global tracer concentrations (and associated uncertainties) in the ocean interior at annual resolution (1940 to 2021). The spatial resolution includes 50 neutral density levels that span the water column along WOCE/GO-SHIP lines. The reconstructed tracer concentrations return a global view of CFCs and SF_6 spreading into new regions of the interior ocean, such as the deep north-western Pacific. For example, they capture the southward spreading and equatorial recirculation of distinct NADW components, and the spreading of CFC-rich AABW out of the Southern Ocean and into the North Pacific, East Indian, and West Atlantic. The reconstructed tracer concentrations fit the data in most locations ($\sim 75\%$), indicating that a steady-state circulation holds for the most part. Discrepancies between the reconstructed and observed concentrations offer insight into ventilation rate changes on decadal timescales. As an example, we infer decadal changes in Subantartic Mode Water (SAMW) and find an increase in SAMW ventilation from 1992 to 2014, highlighting the skill of the time-correction method in leveraging the sparse tracer observations.

Plain Language Summary

The penetration of chlorofluorocarbons (CFCs) and sulfur-hexaflouride (SF_6) into the oceans represents an opportunity to estimate the ventilation rate of the global ocean more directly than other seawater properties. Properties like temperature and salinity are nearly in balance with the ocean circulation and thus are challenging for finding rates of motion, but CFCs and SF_6 are transiently evolving due to a great increase in atmospheric concentrations since 1940. However, the analysis of CFCs and SF_6 also poses challenges, as they are observed infrequently and they have not had time to permeate the entire global ocean. Here, we analyze over $\sim 10^6$ CFC and SF_6 observations that have been taken over four decades, permitting the largest fraction to date of the global ocean to be analyzed using these tracers. A time-correction method is developed to address the temporal sparsity of the observations and an eight-decade annually-resolved picture of CFCs and SF_6 evolution is produced. Roughly 75% of the observations can be explained by the large-scale, statistically-steady ocean circulation acting on the anthropogenically-driven time varying atmospheric concentration.

1 Introduction

The formation and sinking of intermediate-to-abyssal waters, their pathways in the ocean interior and the amount of time they remain sequestered below the mixed layer are key aspects of the ocean circulation that regulate the exchange of heat, anthropogenic carbon and other tracers between the atmosphere and the deep ocean. Since the 1930s, the atmospheric concentrations of chlorofluorocarbons (CFCs), including CFC-11 and CFC-12, and sulfur-hexafluoride (SF_6) have varied significantly following their usage as industrial compounds (Figure 1). Their time-dependent atmospheric input histories are well known and they are conservative in the ocean interior, two characteristics that make them an excellent tool to trace water formation and pathways and to infer ocean ventilation rates (J. Bullister & Weiss, 1983; Smethie Jr, 1993; Rhein, 1994; Orsi et al., 1999; Rhein et al., 2004; Smethie Jr & Jacobs, 2005; LeBel et al., 2008; Tanhua et al., 2009; Rhein et al., 2015; Rivaro et al., 2015; Purkey et al., 2018). Furthermore, transient tracers have been used to quantify the sequestration and spreading of other climatically im-

portant tracers, such as anthropogenic carbon (Sarmiento & Sundquist, 1992; Matear & McNeil, 2003; Khatiwala et al., 2009; Fine, 2011; Ríos et al., 2012; Murata et al., 2019; Mahieu et al., 2020).

CFCs and SF_6 have been measured in the ocean since the 1980s along the major hydrographic sections (Gouretski & Koltermann, 2004; Hood et al., 2010) and used to infer deep-water formation rates and pathways in the Southern Ocean (Orsi et al., 1999, 2001, 2002; Smethie Jr & Jacobs, 2005; Rivaro et al., 2015) and North Atlantic (Weiss et al., 1985; Smethie et al., 2000; Smethie Jr & Fine, 2001; Doney & Bullister, 1992; Azetsu-Scott et al., 2003; LeBel et al., 2008; Tanhua et al., 2009; Rhein et al., 2015). In addition, a number of previous studies have used CFCs to constrain how ocean properties at the surface are connected with those in the ocean interior. This connection is sometimes represented by a Transit Time Distribution, i.e., the probability density function of the transit times since a water parcel was last in the surface mixed layer. The Transit Time Distribution defines the water age at a specific location by representing the advection, mixing and turbulent diffusion of the water parcels that start somewhere at the surface and get to a given interior location. It is often referred to as age spectrum, age distribution, transit-time probability density function, boundary propagator or the Green's function for boundary conditions (Hall et al., 2002). Hereafter, we refer to the Green's function (GF) as the distribution connecting a density class surface points with the ocean interior.

The GF is the solution of an underdetermined problem, and thus requires information beyond that from transient tracer observations. One solution method is found by requiring the shape of the GF to be an Inverse Gaussian function described by just two parameters (mean and width), and the resulting solution is consistent with advection and diffusion in one or two dimensions (Waugh et al., 2003, 2004; Hall et al., 2002, 2007). The assumption of an Inverse Gaussian, however, does not strictly hold in three dimensions when disparate water masses mix (Trossman et al., 2014). The Maximum Entropy method addresses this issue by adding an additional entropy constraint that renders the solution unique while providing as little non-observational information to the problem as possible (Khatiwala et al., 2009; Holzer et al., 2010; Khatiwala et al., 2012), but at the cost of a large computational burden. The limitations listed above call for a method that minimizes the effect of using an Inverse Gaussian as initial guess while analyzing a few hundreds thousand observations simultaneously and while preserving computational efficiency.

This study presents a novel method that solves for the GF and reconstructs the time evolution of CFCs and SF_6 concentrations along hydrographic sections in the global ocean. With now four decades of data, for any given year in which CFCs or SF_6 observations are available, they provide useful information that can be used to constrain the ocean circulation. The result is a steady-state GF that minimizes the misfit between reconstructed and observed tracer concentrations. This solution incorporates not only the large-scale geostrophic flows that can be inferred from inverse solutions (e.g. Reid (1994, 1997, 2003); Talley et al. (2003); Lumpkin and Speer (2007)) but also the net effect of any small-scale advective and diffusive transports. Moreover, the TCM allows us to quantify the reconstruction uncertainty, which have often not been accounted for in inverse solutions (e.g Reid (1994, 1997, 2003)). Finally, through the assumption of a steady-state GF, we can reconstruct tracer concentrations from the first time they entered the ocean in 1940s even if observations were not available. We will refer to this method as the *Time-Correction Method* (TCM), in the vein of Orsi et al. (1999) and as proposed by Purkey et al. (2018). Orsi et al. (1999) produced a map of CFC-11 concentrations by "correcting" CFC-11 observations over the 1984-1996 period, i.e. normalizing them to a mid-term year to minimize the temporal biases.

The annually-resolved reconstruction of tracer concentrations addresses the temporal sparsity of anthropogenic tracer ocean data, which poses large uncertainty in the

assessment of the timescales of physical processes and the ocean circulation variability. For example, formation rates inferred from tracer inventories are inevitably inaccurate because they need to assume observations are synoptic (e.g. Orsi et al. (1999); Willey et al. (2004)). Furthermore, only a few studies (Huhn et al., 2013; Waugh et al., 2013) to date have used CFCs to infer variability in ocean circulation and ventilation, partly owing to the temporal sparsity of observations, with most sections having decadal occupations at best. With the TCM, we investigate how well a steady-state circulation explains the observed tracer concentrations and gain insights into the decadal variability of water mass properties in the ocean interior.

The TCM theory and its skill (and error estimates) in reconstructing CFCs and SF_6 concentrations across the global ocean are presented. A description of the data used and the TCM theory are described in Sections 2 and 3, respectively. The results (Section 4) (i) test the TCM with synthetic data, (ii) present the time corrected CFCs observations in the global ocean including a discussion of deep water pathways, and (iii) discuss the error and potential for this method to constrain decadal variability in ventilation rates. We conclude by discussing future applications of the TCM.

2 CFC and SF_6 observations

2.1 Atmospheric histories

Atmospheric concentrations of anthropogenic tracers CFC-11, CFC-12, and SF_6 have been well monitored since the late 1970s, with reliable reconstructions extending the time series back to the 1930s (Figure 1a). CFC-11 and CFC-12 atmospheric concentrations increased almost linearly between the late 1930s and the 1990s, from when they slowly started decreasing following the regulation by the Montreal Protocol in 1987 (Figure 1a). Emissions of SF_6 started in 1950s and have been increasing steadily since, with a linear increase since mid-1980s (Figure 1a). The atmospheric concentrations of CFC-11 and CFC-12 have been directly measured since 1979, and they were reconstructed prior to that by knowing the industrial production data and the atmospheric lifetimes of their compounds, with uncertainties being a few percent (Prinn et al., 2000; Walker et al., 2000; Fine, 2011). Similarly, atmospheric concentrations of SF_6 have been measured since 1953, and reconstructed by Maiss and Brenninkmeijer (1998) prior to that (Fine, 2011). Here, we use the annual global mean reconstructed atmospheric histories by J. L. Bullister (2015) up to 1977 (1995 for SF_6) and the measured atmospheric values from the NOAA Halocarbons and other Atmospheric Trace Species (HATS) monitoring laboratory (https://gml.noaa.gov/hats/) through 1978-2021.

2.2 Oceanic observations

A global data set of hundreds of thousands of high quality oceanic dissolved tracer measurements has been taken since the late 1970s. Many of these observations were taken along repeated transoceanic full depth hydrographic sections, occupied originally as part of the World Ocean Circulation Experiment (WOCE, Gouretski and Koltermann (2004)), then repeated roughly once every 5-10 years thereafter under the Global Ocean Ship-Based Hydrographic Investigations Program (GO-SHIP, Hood et al. (2010)). The locations of the hydrographic sections discussed or mentioned throughout the manuscript are shown in Figure 1b. Data used here is sourced primarily from the second update of the Global Ocean Data Analysis Project (GLODAPv2.2021) data compilation, which compiles in a single product most of the available shipboard measurements (Lauvset et al., 2021). The GLODAPv2.2021 data is quality controlled but no adjustments have been made to the transient tracer observations. We add data collected during the AnSlope program along the Ross Shelf break (Gordon et al., 2009). Transient tracer observations are accurate within a 5% error (Lauvset et al., 2021) with a CFCs detection limit of 0.01-0.001 pmol/kg and SF_6 detection limit of 0.1-0.01 fmol/kg (Stöven et al., 2015).

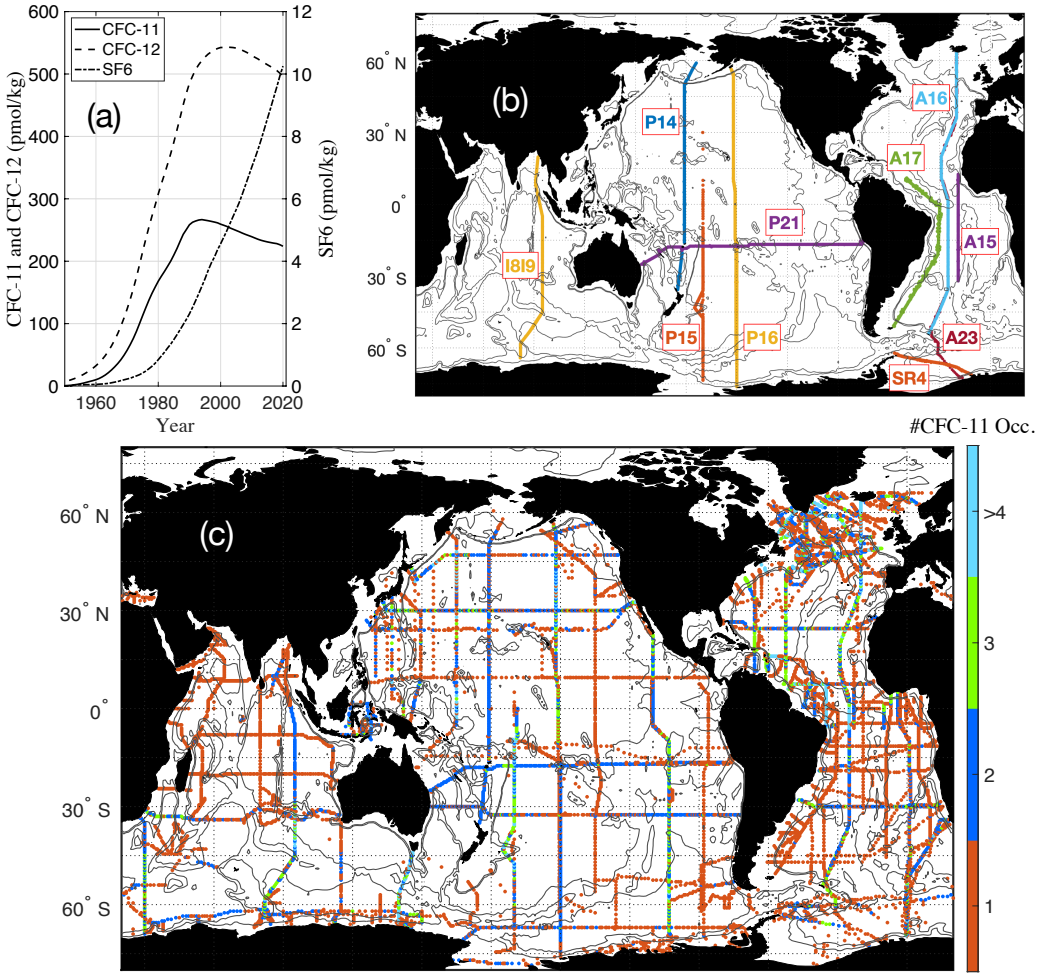

Figure 1. (a) Atmospheric history of chlorofluorocarbon 11 (CFC-11; solid), CFC-12 (dashed) and sulfur-hexafluoride (SF_6; dashed-dotted). (b) Location of key WOCE/GO-SHIP cruises referenced within this manuscript. (c) Number of years with at least one CFC-11 measurement within each 1/2 degree grid cell in waters denser than $\gamma^n = 27$. Thin gray lines indicate the 3000 and 4000 m isobaths.

CFCs and SF_6 observations are distributed globally (Figure 1c). Many sections have been sampled only once, yet a valuable number of observations are available in all ocean basins. In particular, our dataset includes 21,793 and 23,391 casts with CFC-11 an CFC-12 observations, respectively, and 5,724 casts with SF_6 observations. Most stations have 24-36 vertical bottles with higher sampling in the upper ocean. Bottle samples near the seafloor are typically 100 m apart but vary by cruise. Although the method presented here can be applied to any water mass, Figure 1c shows the locations and number of CFC-11 occupations of the observations below neutral density $\gamma^n = 27$ (Jackett & McDougall, 1997), which lies at ∼500 m (global average) and approximately separates the shallower thermocline waters from the deep ocean.

3 Theory

At each location, the tracer surface boundary conditions (C_s) and the tracer concentration in the ocean interior (C) are given by

$$C_s(\mathbf{r}_s, t) = \int_0^\infty C_{atm}(t - \tau_e)\ \mathcal{E}(\mathbf{r}_s, \tau_e)\ d\tau_e, \tag{1}$$

and

$$C(\mathbf{r}, t) = \int_0^\infty C_s(\gamma^n, t - \tau)\ \mathcal{G}(\mathbf{r}, \tau)\ d\tau, \tag{2}$$

where all terms are detailed below. Equation (1) returns the tracer surface boundary conditions at location $\mathbf{r}_s$, where C_{atm} is the tracer atmospheric concentration and τ_e is the air-sea equilibration time. The Equilibration Time Distribution (ETD), $\mathcal{E}(\mathbf{r}_s, \tau_e)$, describes the partitioning of the surface waters according to when they were last in equilibrium with the atmospheric tracer concentration, taking into account the lag-time in surface equilibration due to mixed layer dynamics (see Section 3.1).

Equation (2) describes the propagation of the surface tracer concentration in the ocean interior location $\mathbf{r}$, where τ is the surface-to-interior transit time and $(t - \tau)$ is when a fluid element was last in the surface mixed layer. $\mathcal{G}(\mathbf{r}, \tau)$ is the GF, which partitions the concentration in the ocean interior according to the time when its fluid elements were last in the surface mixed layer. The surface boundary conditions are calculated per each density surface, $C_s(\gamma^n, t-\tau)$, as the average surface condition at the density level outcrop points (see Section 3.1).

Wherever CFCs or SF_6 observations are available, Equations (1) and (2) allow for the reconstruction of the time-dependent interior tracer concentration $C(\mathbf{r}, t)$. The next two Sections describe how to solve for the probability density functions $\mathcal{E}$ and $\mathcal{G}$.

3.1 Solving for the Equilibration Time Distribution

Tracer saturation of the surface mixed layer is temporally variable both in the short and long term; changes in temperature (and thus in solubility), sea-ice formation, and mixed layer processes control the seasonal variations of saturation values, while the long-term growing atmospheric concentration leads to a lag in the equilibration of the surface mixed layer (Rodehacke et al., 2010; Shao et al., 2013). For example, Rodehacke et al. (2010) showed that ignoring the temporal trends in CFC saturation values can lead to up to 10% error in the inventory-based ventilation time-scales.

The ETD partitions the surface tracer concentration according to when it was last in equilibrium with the atmosphere. We parameterize the ETD with a gamma distribution, following DeVries and Primeau (2010), that defines $\mathcal{E}$ as

$$\mathcal{E}(\mathbf{r}_s, \tau_e) = \tau_e^{\theta_e/\beta_e - 1}\ \beta_e^{-\theta_e/\beta_e}\ \left[\Gamma\left(\frac{\theta_e}{\beta_e}\right)\right]^{-1} \exp\left(\frac{\tau_e}{\beta_e}\right), \tag{3}$$

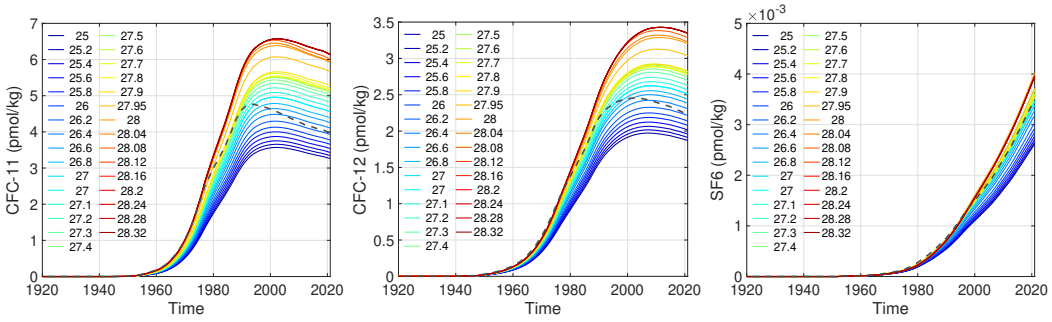

Figure 2. Surface boundary conditions for several density classes for (left) CFC-11, (middle) CFC-12 and (right) SF_6 calculated with the ETD solution (Equation 3). The gray dashed line represent the surface boundary condition obtained with a fixed saturation level (92% and 80% for CFCs and SF_6, respectively) and a fixed solubility calculated with S = 35 and T = 5°C. Note the different scale of the panels.

where Γ is the Gamma function, θ_e is the mean value of the ETD, and β_e is the ratio of the variance of ETD over the mean.

We solve for θ_e and β_e values that minimize the discrepancy between the estimated surface boundary conditions and the tracer observations in the mixed layer. In particular, first the maximum tracer concentration is calculated within the surface mixed layer, defined by using the maximum mixed layer depth (MLD) in the global Argo mixed layer climatology (Holte et al., 2017). This concentration reflects the surface equilibration time under the assumption that winter waters can hold the greatest concentration of the tracers and are preferentially subducted. Such a step is necessary because the seasonal cycle is not resolved by the sparse data. These observations are then used to invert for θ_e and β_e at each location, hence to calculate ETD (Equation 3) and the surface boundary conditions C_s (Equation 1) at each surface location $\mathbf{r}_s$ (wherever tracer data are available).

For each neutral density surface, the average surface boundary condition is calculated by averaging C_s in the outcrop points. For a density level γ^n_*, the outcrop points are defined as all the locations where γ^n_* is lighter than the density at the maximum MLD (see supplementary Figure S1). Note that for waters denser than $\gamma^n = 28.20$, the number of outcrop points with available tracer data rapidly drops (from $\sim 10^2$ points to $<$ 10), and the same surface condition as the closest density layer available is used.

The ETD-based surface boundary conditions used here span a wide range of values (Figure 2). This range is explained by the strongly temperature-dependent solubility used to calculate the surface boundary condition at each location. Solubility is calculated using the average observed temperature and salinity between the surface and the maximum MLD, and using the solubility coefficients and methods reported in Warner and Weiss (1985) for CFCs and J. L. Bullister et al. (2002) for SF_6. Moreover, the roll-off of CFC-11 and CFC-12 surface boundary conditions, following their decrease in atmospheric histories, is delayed in the ETD-based solution when compared with a solution based on a fixed saturation and solubility (dashed gray line in Figure 2). This delay confirms that the ETD approach takes into account the adjustment time of the mixed layer.

3.2 Solving for the Green's function

The TCM is based on solving a non-negative, weighted least-squares problem to find the Green's function, which forces the solution to be strictly positive. Note that we solve for the discrete (annually-resolved) Green's function, $\mathbf{G}$, which is constrained with CFCs and SF_6 up to the age that can be inferred from transient tracers ($\sim$80 years ago). We use a first-guess of the GF, $\mathbf{G}_0$, to constrain our solution for waters older than 80 years, up to 3000 years (see next paragraph).

At each location, the least-squares problem is solved for the optimal $\mathbf{G}$ that fits the existing GLODAPv2.2021 data when convolved with the atmospheric history C_s (see Supplementary Information for more details about the least-squares method used here). We solve for the solution that minimizes the cost function

$$J = ||\mathbf{C} - C_s\mathbf{G}||_2^2 + ||\mathbf{G} - \mathbf{G}_0||_2^2 = \quad (4)$$

$$= (\mathbf{C} - C_s\mathbf{G})^T W^{-1}(\mathbf{C} - C_s\mathbf{G}) + (\mathbf{G} - \mathbf{G}_0)^T S^{-1}(\mathbf{G} - \mathbf{G}_0). \quad (5)$$

At each location, $\mathbf{C}$ is the vector of available tracer observations, C_s is the matrix of the corresponding surface boundary conditions, and $\mathbf{G}_0$ is the first-guess Green's Function. Equation (4) indicates that we look for the solution that (i) minimizes the discrepancy between the GLODAPv2.2021 tracer observations $\mathbf{C}$ and the predicted concentration, i.e. the convolution of C_s and $\mathbf{G}$, and (ii) minimizes the discrepancy between the first guess $\mathbf{G}_0$ and the solved function $\mathbf{G}$. W^{-1} and S^{-1} are the matrices of the weights associated with each one of the terms, respectively (see Supplementary Information for more details).

In particular,

1. W is a diagonal matrix, with $1/max(5\%\mathbf{C}, C_{lim})^2$ on the diagonal. C_{lim} is the observation detection limit (Section 2), for which we choose 0.01 pmol/kg for CFCs and 0.1 fmol/kg for SF_6, a conservative choice of the limits presented in Stöven et al. (2015). 5% of $\mathbf{C}$ represents a 5% error, which is the measurement error associated with transient tracer observations (Lauvset et al., 2021).
2. Our first guess of the GF, $\mathbf{G}_0$, is an Inverse Gaussian whose characteristics are based on the solution of the Total Matrix Intercomparison (TMI) approach described in Gebbie and Huybers (2010, 2012). In the TMI method, several tracers (temperature, salinity, nitrate, phosphate, silica and oxygen isotope) are used to invert for the ocean circulation and radiocarbon is used to infer water ages. For clarity, radiocarbon is used only in the first guess $\mathbf{G}_0$ and not to deconvolve our final GF. Given that our final GF uses 'young' tracers, our solution tends to relax to the first guess GF for ages older than the eight decades constrained by CFCs and SF_6.
   To construct the first guess GF at each location, we use the water age estimated by the TMI method (Γ_{TMI}) to produce an ensemble of Inverse Gaussians: the ensemble is generated by varying Γ_{TMI} with a normal distribution, assuming a factor of 2 of confidence of Γ_{TMI} and a ratio $\Delta/\Gamma = 1$, as consistent with tracer observations (Waugh et al., 2003, 2004; Hall et al., 2004). Errors in Γ_{TMI} are probably no larger than 100-200 yrs for the oldest waters and less for younger waters (Gebbie & Huybers, 2012), but here we conservatively assume that Γ_{TMI} is uncertain to a factor of 2 to avoid over-constraining our solution of $\mathbf{G}$. The first guess $\mathbf{G}_0$ is an Inverse Gaussian calculated as the ensemble average. This approach is summarized in Supplementary Figure S2.
3. The level of confidence of the first guess $\mathbf{G}_0$ is given by the covariance of the Inverse Gaussians ensemble. It follows that $S^{-1} = (\mathbf{G}'\mathbf{G}'^T)^{-1}$, where $\mathbf{G}' = \mathbf{G}_i - <\mathbf{G}_i>= \mathbf{G}_i - \mathbf{G}_0$, $\mathbf{G}_i$ is the i-th Inverse Gaussian of the ensemble, and $\mathbf{G}_0 =<\mathbf{G}_i>$ is the ensemble average. In solving for $\mathbf{G}$, we do not want our first guess to constrain the solution to a prescribed shape. In other words, our priority is to

fit the available observations rather than fitting $\mathbf{G}_0$ (Equation 4). Therefore, if our solution does not fit the observations within a 5% error, the weight of the first guess S is reduced until the mismatch error is reduced within the 5% error limit or when the data fitting does not improve anymore.

In summary, for each location where tracer concentrations are available, we make use of knowing (i) the tracer observations $\mathbf{C}$ and (ii) the surface boundary conditions C_s, to solve for the boundary GF $\mathbf{G}$ at annual resolution.

3.3 Applying the TCM to oceanic tracer data

At each station, the GLODAP oceanic tracer data (Section 2) is first vertically interpolated onto a uniform neutral density grid with spacing of $\Delta\gamma^n = 0.01$. The interpolation uses a piecewise cubic Hermite interpolating polynomial and depth-separation limits to avoid interpolating between points too far away for the interpolated value to be deemed acceptable, following Key et al. (2010) (see their Table 4; depth-separation limits used here are the more conservative values reported for the Arctic Ocean). All stations taken within one year and within a single 1/2° horizontal resolution WOCE grid are binned by taking the mean at each density level.

The TCM is applied to every 1/2° x 1/2° grid box and density level where at least one transient tracer observations exists (Figure 1c). Note this analysis does not return a three-dimensional gridded product yet, but the spatial interpolation in locations where tracer data is missing is part of ongoing work. All available tracer observations at each grid box is used to constrain our solution for GF (see details in the Supplementary Text S1). Then the GF is used to reconstruct the time-dependent tracer concentration in the ocean interior following Equation (2) by convolving the GF with the surface boundary conditions resulting in an estimate of the CFC-11, CFC-12 and SF_6 concentration for each year between 1940 and 2021. Error estimates of the time-corrected tracer concentrations are also calculated as 95% confidence limits.

4 Results

4.1 Testing TCM skill with synthetic data

Synthetic data is used to test the TCM performance in (i) deconvolving the GF and (ii) predicting the tracer concentration and its associated error, and to analyze its sensitivity to the number of observations and tracers available. We start by assuming a known true GF, for which we use an Inverse Gaussian (Figure 3, black curve) and a bimodal function generated by combining two different Inverse Gaussian functions (not shown but results are qualitatively similar to Figure 3). In these tests, we assume a fixed surface boundary condition, as represented by the gray dashed lines in Figure 2 and use the known GF to predict the *true* tracer concentrations in the ocean interior (thick colored lines in the right sub-panels). To test the TCM, we sub-sample the true tracer concentrations, add random error (up to 5%) that represents contamination of the signal by noise, and deconvolve the GF. We use an initial-guess GF as described in Section 3.2 (dashed line). The resulting estimated $\mathbf{G}$ (dash-dotted line) and predicted tracer concentrations (thin colored curves) for various sampling scenarios are shown in Figure 3.

The TCM reproduces the known tracer concentrations within error for all tested scenarios (Figure 3). We start by showing the limiting case of only one tracer (CFC-11) observation at one time (panels a and b). The TCM prediction fits the available (contaminated) observation perfectly, i.e. tends to overfit the solution given the underdetermined nature of the problem. The TCM-solved GF is smooth and very close to fitting the true GF, indicating that the first guess is helping constrain the solution. The tracer prediction is also consistent with the true tracer concentration for all the tracers, includ-

ing the tracers not used to solve the GF (CFC-12 and SF_6). The prediction is closest to the truth near the observation, with a slight underestimate toward the end of the time period. However, the true concentrations are within the errorbar limits of the TC solution at all times. Note that even the error estimates (95% confidence limits) of CFC-12, which is not used in this scenario, are nicely constrained by the CFC-11 error estimates due to the similar atmospheric histories of these transient tracers.

The second scenario, again tests the method with only one observation, but now considers when the observation is only available either early (blue) or late (red) in the time frame (Figure 3b). The TCM's GFs are only slightly different and the tracer predictions are within the error bars of the true concentration in both cases. As in the first scenario, the error bars become larger the further away from the time of the observation. The bias between the reconstructed and 'true' tracer concentrations, i.e. whether the reconstruction is larger or smaller than the truth, is determined by the sign of the contamination of the 'true' observations and by the fixed surface boundary conditions. In the examples of Figure 3b, when the observation is available only late in the predicted time frame, the method slightly overestimates early tracer values; and when the observation is only available early, the method slightly underestimates true concentrations toward the end of the time frame.

In scenario three, again we allow only observations at one instance, but provide the TCM with three tracers (CFC-11,CFC-12,and SF_6) (panel c). Having all three tracers at the same time improves the predictive power of the method and reduces the error estimates, in particular for the newly added tracer (SF_6 in this example, compare the errorbars in panels a and c).

Finally, in scenario 4, we show that the method's skill improves as we increase the number of available observations (panel d). When two (or more occupations, not shown) samples are taken 1 decade or more apart, error bars are reduced by 30-50% (panel d VS a), showing increased level of confidence in our reconstruction.

4.2 Reconstructed transient tracer distributions

The reconstructed global data set of annual concentrations of CFC-11, CFC-12, and SF_6 paints a more detailed picture of ocean ventilation and deep water circulation than previously possible with observations alone. High CFC-11, CFC-12, and SF_6 values are found in the upper ocean due to the effective ventilation by the wind-driven circulation, as expected. Regions of the deep and abyssal waters also have high values, especially those that have been in contact with the atmosphere within the last decades. Analyses of the time varying concentrations following these CFC-rich water-masses meridionally provide direct observations of time scales of ocean transport. In addition, the solved GFs allow for direct assessment of the mean age and age distribution of interior water throughout the global ocean. We focus on a global description of the data set, highlighting its key scientific applications. Given the assumptions in the boundary conditions, this product is expected to best reproduce large-scale patterns, although the same method could be applied in the future to regional problems.

The reconstructed tracer concentrations along three WOCE meridional sections that span the Atlantic (A16+A23), Pacific (P16) and Indian (I08S+I09N) are used to demonstrate the time evolution of the tracers meridionally and to allow direct comparison between basins by adjusting GO-SHIP data to the same year. Along each of the sections, grid boxes nominally following the cruise tracks were selected (see Figure 1b for their location). For each year, the reconstructed values of CFC-11, CFC-12 and SF_6 where objectively mapped in latitude-depth space using decay scales of 40 km and 1 km in the horizontal and vertical directions, following Roemmich (1983). The reconstruction of CFC-11 concentration through 2021 is shown in Figure 4, while complementary reconstruc-

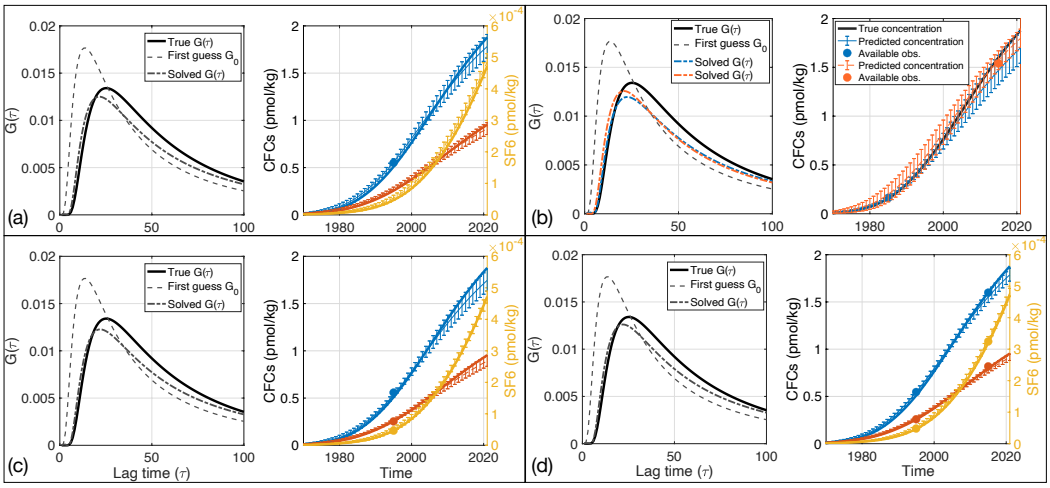

Figure 3. Results from four TCM performance tests with synthetic data. Per each sub-panel: right panels show the GFs, including the True GF (black), first guess $\mathbf{G}_0$ (dashed gray line) and predicted GF solved using the TCM (dash-dotted black line); left panels show the tracer concentrations, CFC-11 (blue), CFC-12 (red), SF_6 (yellow). Thick tracer lines are the true tracer concentrations and the thin lines are the predicted values using the TCM with associated error estimates (95% confidence limits). Colored dots indicate the sub-sampled "observations" used for the TCM prediction.

tions of CFC-12 and SF_6 concentrations are shown in Supplementary Figures S3 and S4, respectively.

4.2.1 Antarctic Abyssal Water

Antarctic Bottom Water (AABW) is primarily produced along the Antarctic shelf where dense shelf waters entrain ambient waters as it flows down the continental slopes (e.g. Jacobs et al. (1985); Gordon (2019)), and is returned to shallower depth via cross-density mixing, which leads to a net dense-to-light water mass transformation. High tracer values are observed at the bottom near and directly downstream of all four AABW production regions (Figure 5). The Weddell Sea, one of the primary sites of export of dense shelf waters, is highlighted by the large CFC-11 values at 70-55°S in the Atlantic Ocean along the northern edge of the gyre where recently formed water on the shelf are advected clockwise around the gyre (Figure 4a and Figure 5; (Orsi et al., 1999)). Somewhat large values are also found in the southern edge of the gyre located east of the primary AABW formation region, indicating newly formed deep waters either coming from further east near Cape Darnley or the return of the Weddell Sea Deep Waters having made a full circle around the gyre, while minimum CFC-11 concentrations are found in the middle of the gyre. The reconstructed CFC-11 concentrations along SR03 to the east(not shown, see Figure 1b for location) include values up to 0.5 pmol/kg everywhere below 2000 m across the gyre, and even larger values along the northern boundary, confirming the significance of the gyre circulation in transporting AABW, as shown by the deep pathways suggested in Figure 4a.

As AABW flows northward in all ocean basins, it is strongly constrained by topography and often channeled through passages or fracture zones. In the South Atlantic, CFC-11-rich AABW has propagated northward all the way to the equator. The signal in Figure 4a is clear only up to 10°N, but A16 does not well capture the core of the northward flow along the west boundary. The northward propagation of CFC-11 within AABW

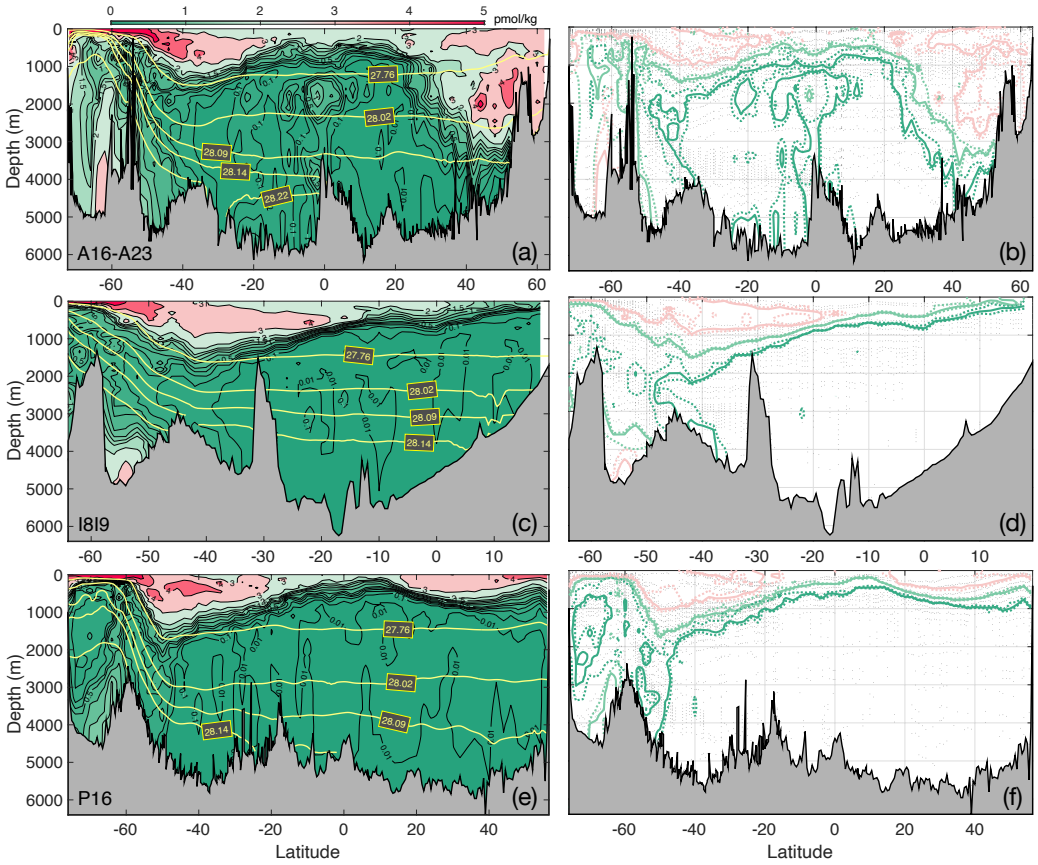

Figure 4. Reconstructed CFC-11 concentrations along A16+A23 (panels a,b), I8I9 (c,d), and P16 (e,f) in 2021. Panels in left column show the reconstructed concentration and neutral density contours (yellow) along each section. Panels in right column show the observation locations throughout all decades of available data (gray dots) and the uncertainty of the time corrected CFC-11 concentrations for three contours (0.2, 1 and 3 pmol/kg). The solid line shows our best estimate, while the dotted lines show the 95% confidence limits.

density layers is better seen along A17 (not shown), although with some more noise due to the low number of observations available along this section, in particular at depth. In previous estimates from 1990s data (Orsi et al., 2002), the detection limit contour of 0.01 pmol/kg did not extend farther than 40-35°S, where now we reconstruct values up to 0.15-0.2 pmol/kg. The only locations where CFC-11 reconstruction is predicted to be below detection limit in 2021 within the AABW layer in the Atlantic Ocean is east of the Mid-Atlantic ridge in the very north and southern parts of the basin (Figures 4a and 5). Here, the first few hundred meters above the seafloor are mainly occupied by AABW (G. C. Johnson, 2008), and hence our result is consistent with a slow abyssal circulation in the eastern Atlantic after crossing the Romanche Fracture Zone. This result is highlighted by the CFC-11 bottom arrival time i.e., the year in which CFC-11 concentrations first exceeded the detection limit at the ocean bottom (Figure 5).

In the Indian Ocean, high CFC-11 concentrations are found in the Princess Elizabeth Trough and Antarctic-Australian Basin, which I8I9 crosses between 50-80°E. Here, our reconstruction captures high CFC-11 both on the southwest and northeast flanks of the basin, consistent with Ross-formed and Adelie-formed AABW flowing in from the southeast (i.e. directed northwest), looping within the basin and flowing back southeast (Figure 5). We also find values well above detection limit up to 30°S, indicating that CFC-11-rich AABW waters have crossed the Antarctic-Australian Discordance at 50°S and are moving northward along the Southeast Indian ridge. Further north, our reconstruction displays minimum values between 2000-4000 m, and values above detection limit both above and below, suggesting AABW waters carrying CFC-11 could have already travelled all the way to the equator. Note however we only rely on a limited number of observations north of 30°S at depth (Figure 4d), so the conclusion on how far north AABW has spread in the Indian Ocean still needs caution.

The deep Pacific Ocean is mostly filled with Ross Sea-formed and Adelie Coast-formed AABW (Solodoch et al., 2022), consistent with the high CFC-11 values through the Bellinghausen Basin (between 60-65°S in Figure 4e) and its spreading through the Southwest Pacific Basin, with values up to 0.1 pmol/kg up to 50°S. Within the Pacific, the highest deep CFC-11 values are found along the western boundary of the basin sampled by the P15 section, tracing the northward path of AABW that flows as a Deep Western Boundary Current hugging the Campbell Plateau (see Figure 1b for location and Figure 5 for the earlier arrival time of AABW along P15). The core of northward AABW flow in the western Pacific around Campbell Plateau continues northward offshore of the Kermadec and Tonga trenches and flows in the north Pacific channel through the Samoan Passage (Figure 5). Our reconstruction returns a clear signal of AABW crossing the Samoan Passage (P21, Figure 6a) in the late 90s-early 2000s and moving northward (P14, Figure 6b) in the early-to-late 2000s.

4.2.2 North Atlantic Deep Water

The Atlantic Ocean interior is mostly filled with North Atlantic Deep Water (NADW), formed in the Labrador Sea and Nordic Seas of the North Atlantic. NADW flows southward above the denser AABW throughout the Atlantic Ocean (spanning depths of ∼1000-4000 m) and re-surfaces in the Southern Ocean mostly through wind-induced Ekman pumping (Talley et al., 2003; Lumpkin & Speer, 2007; Talley, 2008; Smeed et al., 2014; Cessi, 2019; H. L. Johnson et al., 2019). The North Atlantic, through the formation and southward spreading of NADW, constitutes the largest CFC-11 inventory in the global ocean (Supplementary Figure S5; see also Willey et al. (2004)). A clear CFC-rich NADW core is observed down to 40°N along A16 and 30°N within the western NADW boundary current to the west (Figure 7). These high CFC values (up to 3 pmol/kg) were not found South of 50°N in previous reconstructions of Orsi et al. (2002), who used all the available observations up to the late 1990s.

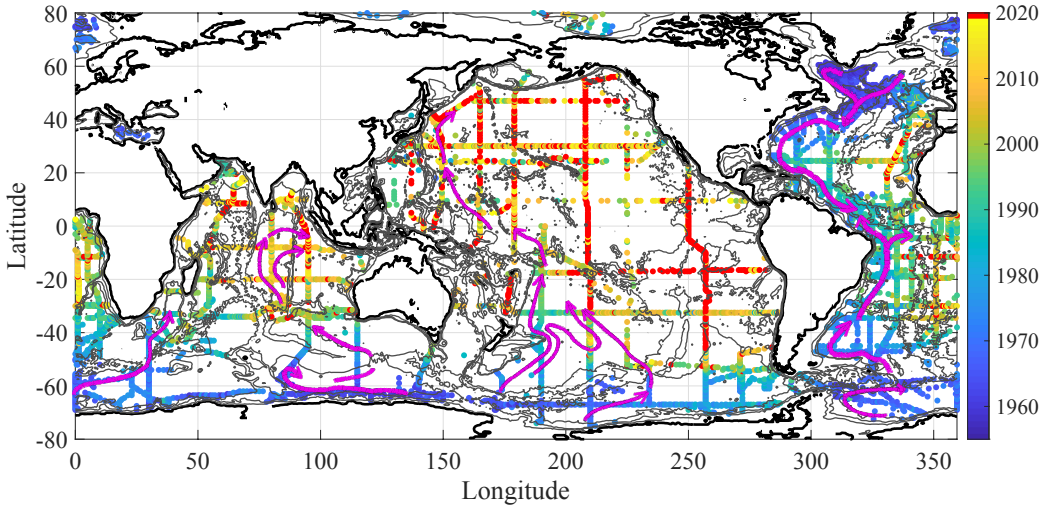

Figure 5. (a) Reconstructed CFC-11 arrival time at the ocean floor. The arrival time is defined as the year when CFC-11 first exceeded the detection limit of 0.01 pmol/kg. Values in red indicate areas where CFC-11 values are still below detection limit. Magenta arrows indicate some of the major AABW and NADW pathways taken from Reid (1994, 1997, 2003).

The Deep Western Boundary Current (DWBC) pathway of the southward flowing NADW is the fastest pathway for NADW to reach the southern hemisphere. To further quantify the time scales of advection, here we show the 10% ventilation time, t_{10}, defined as the time it took to ventilate 10% of the water at each location, namely $t_{10}(\mathbf{r}, t) = \int_0^{t_{10}} G(\mathbf{r}, \tau) d\tau = 0.1$. Figure 7 shows t_{10} on $\gamma^n = 27.90$, which lies at about 2000 m in the middle of the Atlantic Basin and crosses the core of the Labrador Sea Water component of NADW. The 10% ventilation time is better suited to describe younger waters than the mean age, $t_m(\mathbf{r}, t) = \int_0^{\infty} \mathcal{G}(\mathbf{r}, \tau) d\tau$, and so is a better suited expression of the water age on the decadal timescales described by CFCs and SF_6. The broad region where a fast arrival time is found in the subpolar North Atlantic reflects the multiple varieties of dense waters being formed here. While their pathways are not necessarily restricted to the western boundary (Lozier, 1997; Lozier et al., 2022), the 10% ventilation time is shorter (10-30 years) in the western North Atlantic, compared to the eastern Atlantic, where CFCs and SF_6 have barely arrived as of 2021 ($t_{10} \simeq 80$ years).

CFCs and SF_6 are effective in constraining the GFs and minimizing the effect of using an Inverse Gaussian as the first guess. Following NADW as it moves southward, the GFs become increasingly wide, indicating that waters have moved away from the source regions and mixed along the way (Figure 7b). The solved GFs can differ quite substantially from the first guess, and even return bimodal solutions that indicate the contribution of different water masses (solid vs dashed lines in Figure 7b). The 10% ventilation time progressively increases from just 2 years at 56°N to 32 years at the equator. The reconstructed CFC-11 concentration reveals that the high latitudes in the North Atlantic are already experiencing the roll-off in CFC-11 atmospheric history, and even values at 35°N have started plateauing, while CFC-11 are still steadily increasing further south (Figure 7c).

Further downstream, subsurface tracer maxima are found in the equatorial deep Atlantic, where part of the southward flowing NADW turns eastward along the equator (Weiss et al., 1985; Schott et al., 2003; Rosell-Fieschi et al., 2015; Herrford et al., 2017). We observe a CFC-11 minimum sandwiched between a shallow maximum at 1500-2500

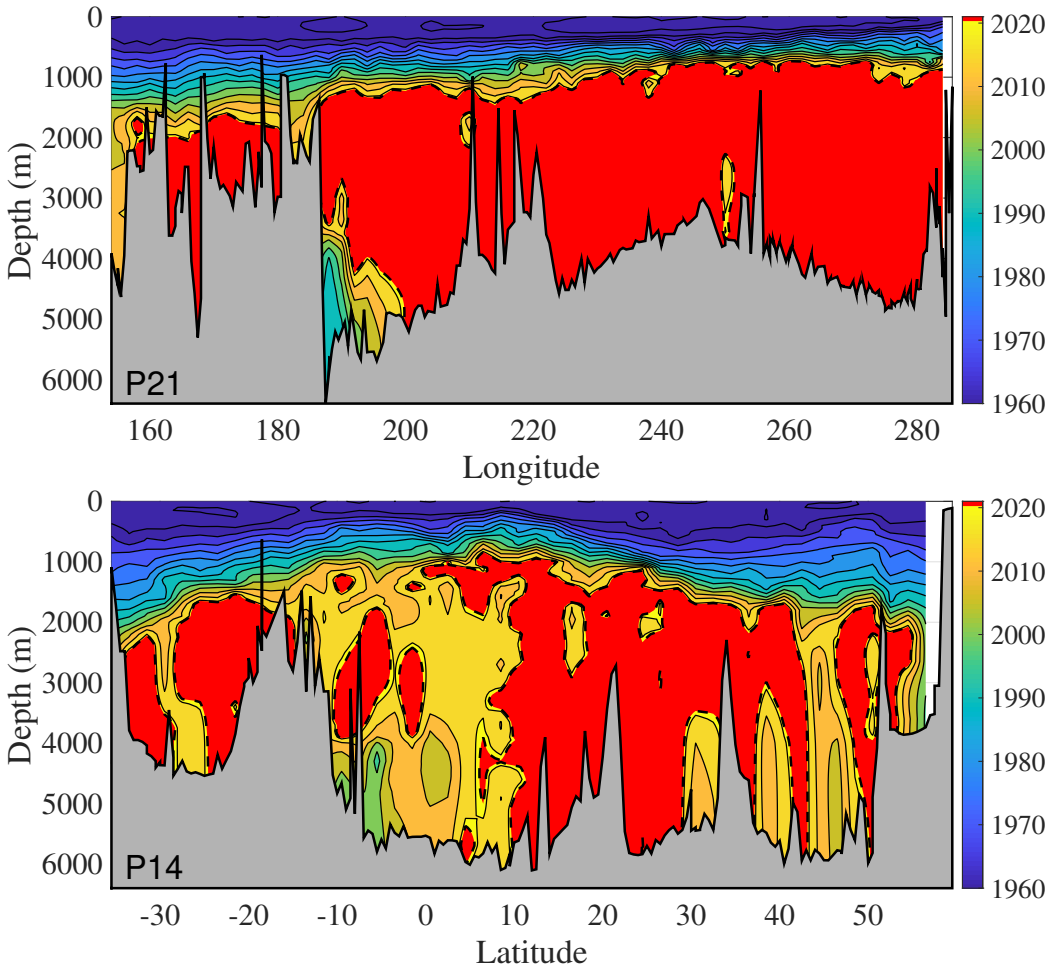

Figure 6. Reconstructed CFC-11 arrival time along P21 and P14 in the Pacific Ocean (see Figure 1b for the location of the sections).

m and a deep maximum at 3200-4500 m. This CFC-11 pattern is consistent with oxygen patterns and transport patterns found in previous studies (Schott et al., 2003; Rosell-Fieschi et al., 2015; Herrford et al., 2017). The maxima correspond to the lighter and denser variations of NADW, known as upper NADW (uNADW) and lower NADW (lNADW), respectively (the neutral density levels indicating the interface between the different components of NADW are displayed in Figure 4a). In between, the CFC-11 minimum is likely caused by an older water mass coming from the southeast, possibly modified or recirculated NADW water (Friedrichs et al., 1994; Rhein et al., 1995; Herrford et al., 2017). The time-corrected CFC-11 concentrations along A17 and A15 sections, which cross the equator at 30°W and 19°W (while A16 crosses it at 25°W), respectively show that the two maxima are more evident further eastward (A15) and less separated further westward (A17), in agreement with tracer dilution being caused by older NADW recirculating from the southeast.

The shallow equatorial CFC-11 maximum (1500-2500 m) was first observed in 1983 (Weiss et al., 1985) and consistently makes its first appearance in the early 1980s in our reconstruction (not shown). The smaller deep maximum (3200-4500 m) was first observed in 1988 (Doney & Bullister, 1992), and again consistently first appears in the mid-1980s in the tracer reconstruction. The core of the deep maximum initially sits within lNADW and spreads between lNADW and AABW within just a few years, potentially because of the large mixing between these two water masses across this region (Herrford et al., 2017). As time progresses, the deep maximum crosses denser density classes, suggesting a delayed contribution of AABW-carried CFC-11. The high CFC-11 equatorial concentrations were only partially evident in Orsi et al. (2002) and in the WOCE atlas (Koltermann et al., 2011), with values still very close to the detection limit used here (0.01 pmol/kg) in the 1990s. The deep CFC-11 maximum, in particular, was nearly undetectable and confined to 4200-4500 m in both estimates, suggesting it was mainly associated with lNADW flow rather than AABW.

4.3 Variability

The TCM finds the best Green's function fit for the whole period of available atmospheric and oceanic observations, implicitly characterizing the circulation as steady. A steady-state circulation, i.e. one for which observations are within the uncertainty errorbars of our reconstruction, is globally capable of explaining 73% of the points within the 95% confidence errorbars, varying some by density class (Figure 8b). Individually considered, the different tracers used here return different levels of misfit between the reconstructed and observed concentrations. About 80% of CFC-11, 70% of CFC-12 and 55% of SF_6 observations are within the 95% confidence errorbars. SF_6 observations are rarely available independently and it could prove more challenging for the method to find a solution that satisfies tracers with different atmospheric histories at the same time, possibly explaining the lower percentage of SF_6 data comprised by the errorbars.

If the TCM solution was always consistent with the available observations, 90% of the reconstructions should be within errorbars, given that errorbars are calculated as the 5% - 95% confidence limits. The lower fit found could be caused by temporal variability in the circulation or by sensitivity to the initial conditions used in the method. An analysis of the spatial (horizontal and vertical) and time distributions of the misfit between the reconstructed and observed concentrations offers insight into where the circulation is not in steady state and can suggest either a slowdown or speed up in ventilation of particular water masses. However, given the spatial sparsity of available observations, a regional approach would be better suited to investigate changes in different water masses where local dynamics can be examined, thus we leave this analysis mostly to future studies, with only one example following on previous studies discussed below. Here, we simply show that the misfit is normally-distributed around zero, i.e. the TCM

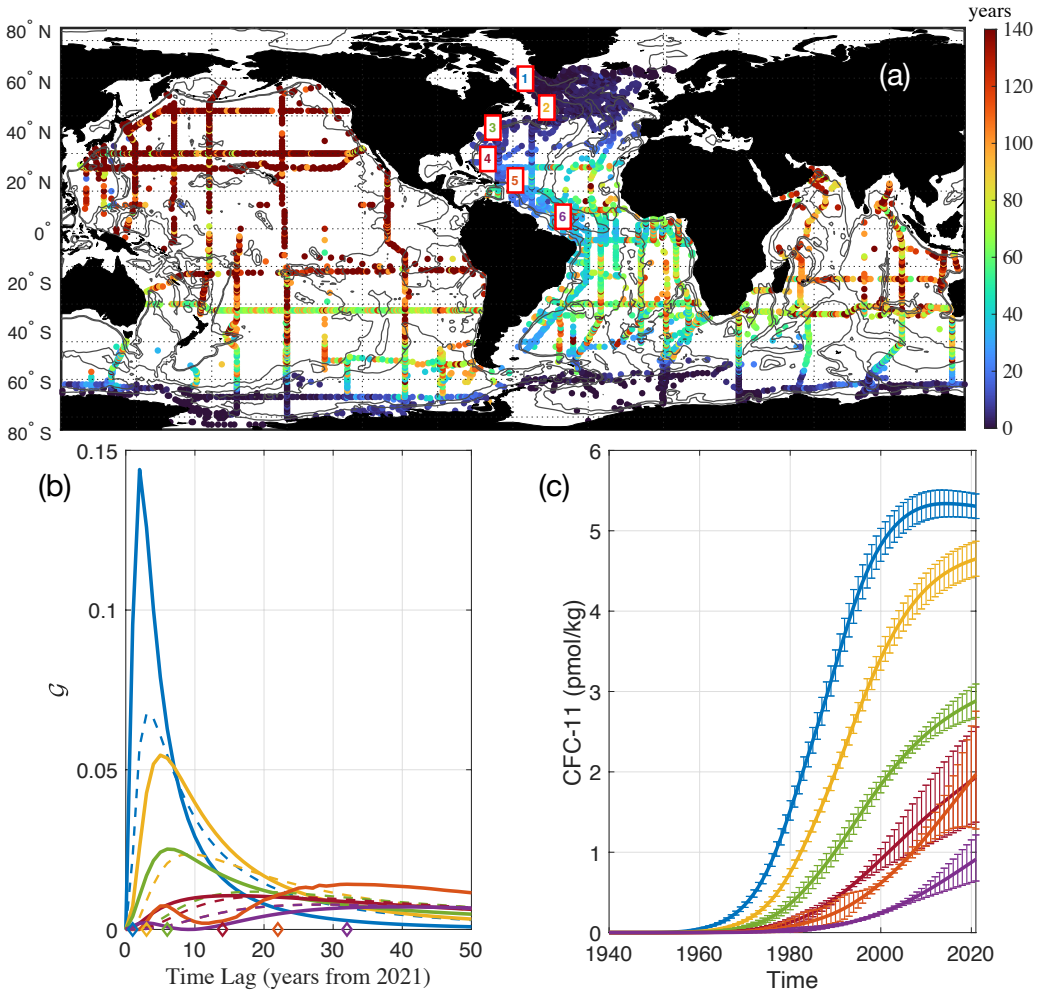

Figure 7. (a) 10% ventilation time on neutral density surface $\gamma^n = 27.90$, the density class that crosses the core of the Labrador Sea Water component of NADW. The Green's functions (b) and the reconstructed tracer concentrations (c) at 6 points (color-coded labels in panel a) across the Atlantic Ocean. The color-coded diamonds at the bottom on panel b indicate the 10% ventilation time (t_{10}) for each of the displayed Green's functions. Dashed lines in panel (b) show the first guess Green's function used per each location (color-coded).

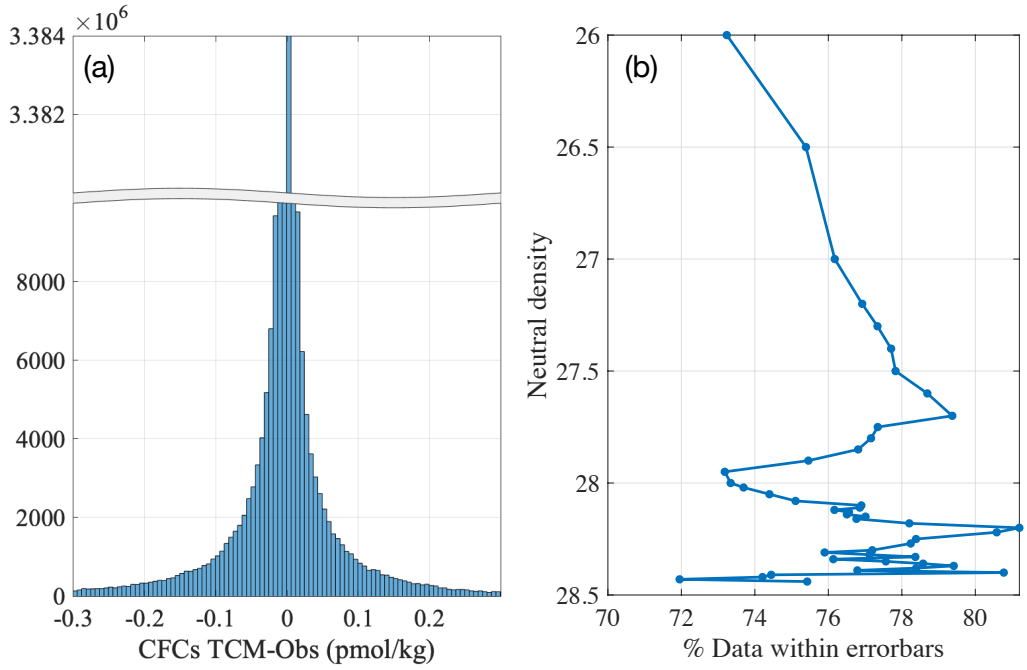

Figure 8. (a) Distribution of the misfit between the reconstructed and observed tracer concentrations, for all tracers and all ocean basins. (b) Globally-averaged percentage of observations within the errorbars of our reconstruction for each density level used in this study.

tracer reconstruction fits the data in most locations, confirming that the steady-state holds for the most part and that there are no biases in the TCM reconstruction (Figure 8a).

4.3.1 Variability in Subantarctic Mode Water

The TCM not only informs us about the steady-state ocean circulation, but offers a quantitative method for assessing decadal ocean variability. The TCM reconstruction fits most of the data (Figure 8a), and it tends to overfit the data when we have only one occupation due to the large underdetermined nature of the problem (Figure 3). Therefore, when we have multiple occupations and the reconstruction does not agree with observations within the error estimates, the null hypothesis of steady-state circulation is rejected and the temporal variability can be assessed.

As an example, decadal changes in the ventilation of Subantarctic Mode Water (SAMW) are discussed. Transient tracer vertical inventories (Figure S5) reveal that a primary area of transient tracer accumulations is the Southern Ocean north of the Sub-Antarctic Front (around 50°S), co-located with the maximum wind-stress curl where SAMW and Antarctic Intermediate Waters (AAIW) are formed. SAMW and AAIW flow northward through the sub-tropical thermocline in all ocean basins, and contribute to the closure of the Atlantic Meridional Overturning Circulation by returning water to the North Atlantic. High CFC-11 concentrations downstream of SAMW and AAIW formation sites are evident across all ocean basins, with values up to 3 pmol/kg spreading up to 20°S in 2021 (Figure 4), a northward propagation of almost 20 degrees latitude from the 1990s (Orsi et al., 2002).

Several studies have used repeat measurements of transient tracers to estimate changes in ventilation rates in the Southern Ocean thermocline waters, and have generally shown a decrease in SAMW age, implying an increase in the ventilation rates (Tanhua et al.,

2013; Waugh et al., 2013; Fine et al., 2017; Ting & Holzer, 2017; Morrison et al., 2022). Here, we compare the reconstructed and observed concentrations along section P16, in analogy with the past studies cited above.

The comparison of the reconstructed and observed tracer concentrations suggest an increase in SAMW ventilation rate from 1992 to 2014. The TCM analysis solves for the GF that best fits all occupations (1992, 2005 and 2014). If the circulation is changing linearly in time, the solution would be roughly centered in the mid-term of the considered period, in this example ∼2003, explaining why the differences between reconstructed and observed concentrations are smallest in 2005 (Figure 9b). The reconstructed concentrations in SAMW [1] in 1992 are slightly higher than observations (Figure 9a), while they are lower than observations in 2014 (Figure 9c). On the other hand, the reconstructed CFC-11 concentrations in the Circumpolar Deep Waters (CDW [2]) reveal the opposite pattern, namely they are lower than observations in 1992, and higher than observations in 2014 (Figures 9a,c).

To further confirm the differences described above, we repeat the TCM analysis using only the 1992 data to predict the 2005 and 2014 (Figure 9d-f), as it has been done in Waugh et al. (2013). While the GFs used to predict the tracer concentrations are different, the idea is the same: the prediction assumes steady-state circulation and divergences between reconstructed and observed concentrations suggest ventilation rate changes. In this scenario, the anomalies between the reconstructed and observed CFC-11 in 1992 are naturally small (close to zero), confirming that the TCM finds a solution that fits the available data (Figure 9d). The tracer differences in 2005 confirm the patterns shown in Waugh et al. (2013), i.e. lower (larger) reconstructed concentrations in SAMW (CDW) than in observations (Figure 9e). The tracer differences in 2014 shows a further decrease (increase) in SAWM (CDW) ventilation, showing a continuation of the trend discussed in Waugh et al. (2013). In 2014, the differences between reconstructed and observed concentrations are qualitatively similar whether we employ all available occupations simultaneously or 1992 observations only (Figure 9c,f).

The increase in SAMW ventilation rate has been linked to the intensification and poleward shift of the westerly winds around Antarctica (Waugh et al., 2013). Stronger winds would lead to an increase of the upper overturning circulation, i.e. a stronger export of SAMW and more upwelling of the older, tracer-poor CDW. While this mechanisms could explain the observed changes, other processes could have caused similar changes in ventilation (e.g. changes in the subtropical gyres, see Morrison et al. (2022)), challenging the attribution to a single mechanism. Despite these attribution difficulties, the changes have been determined with a number of different methods in different studies, suggesting that they are not the result of uncertainties in estimates of the tracer concentration (or age changes), but rather the result of variability.

5 Summary and Discussion

Transient tracers have played a critical role in advancing our understanding of ocean circulation and ventilation, but direct quantitative interpretation of their presence can be challenging owing to (i) the non-linearity of their time varying atmospheric history, (ii) unknown surface saturation, and (iii) the complicated competition between advection and mixing in the ocean interior (Purkey et al., 2018). Here, we present a new mathematical framework that leverages the global data set of CFC-11, CFC-12 and SF_6 data to solve for the steady-state age distribution and the annual concentration of each tracer between 1940 and 2021 at every location where tracer data exists in the interior ocean.

[1] SAMW: $\gamma^n = 26.6 - 27.2$ and north of the Sub-Antarctic Front at ∼50°S
[2] CDW: $\gamma^n = 27.2 - 27.6$ south of the Sub-Antarctic Front

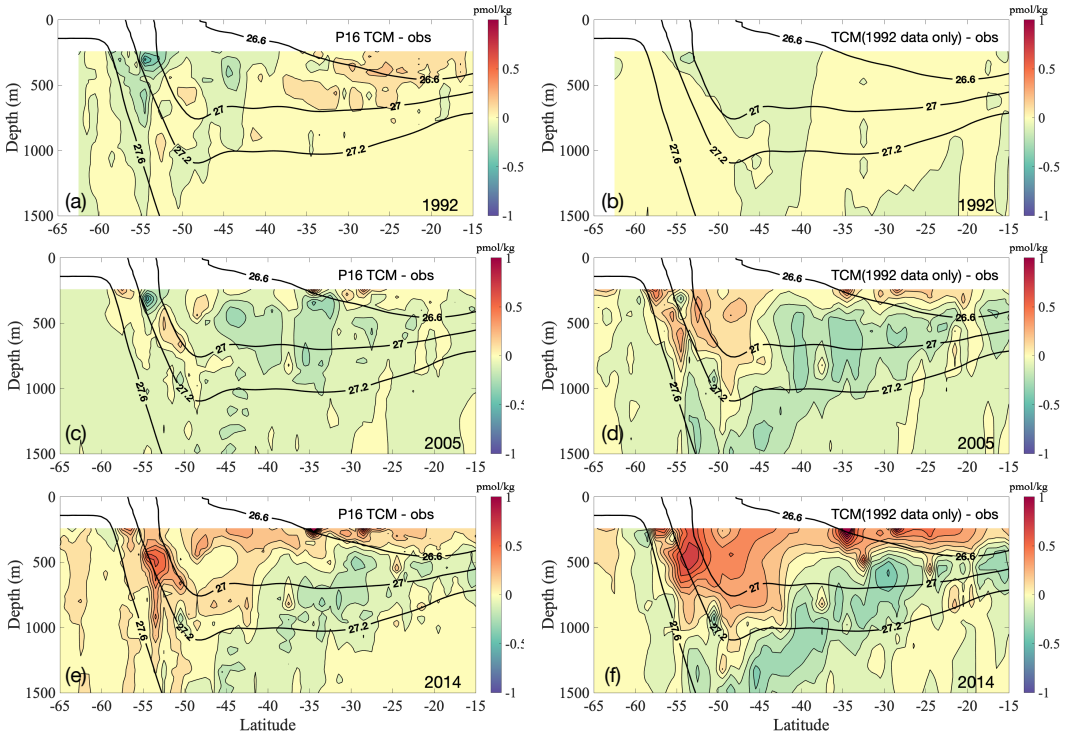

Figure 9. Depth-latitude cross sections of the difference between reconstructed (TCM) and observed CFC-12 concentrations for repeat cruises along P16 (shading) and potential density (σ_0) contours at the section location (black contours). Left panels: reconstructed concentrations are estimated using all available data (three occupations, in 1992, 2005 and 2014). Right panels: reconstructed concentrations are estimated using 1992 data only.

This global, annual, tracer dataset allows for evaluation of the mean circulation of the deep ocean and time scales of ventilation. In addition, this new dataset can be used to validate ocean models (Solodoch et al., 2022). Furthermore, comparison of the steady-state reconstructed tracer concentration with the observed concentrations allows for direct assessment of where ocean ventilation has varied over the 1940-2021 period, with potential implications for the rate of ocean heat and carbon uptake.

The Time Correction Method presented here leverages the longer record of CFCs and SF_6 that is now available. The further expansion of these tracers into deep ocean permits a more direct inference of ventilation time for a greater fraction of the global ocean. In addition, the atmospheric histories of CFC-11, CFC-12, and SF_6 have diverged over the last few decades, and thus these tracers now provide more independent constraints regarding ocean circulation. The time correction method doesn't restrict the age distribution of the interior ocean to follow a prescribed Inverse Gaussian distribution that describes the evolution of a single water mass. The combination of the time-correction method with a longer timeseries of data leads to more complicated descriptions of the circulation to be inferred, such as bimodal age distributions that correspond to the isopycnal mixing of two water masses with different histories.

The findings presented here come with some known caveats, including some due to the use of surface boundary conditions in discrete density classes constrained by the available observations within the geographical region where that density outcrops. Especially for some of the deep density layers formed seasonally under ice where there is extremely limited data, the saturation value is uncertain, however, an inference based on the closest observations is likely more accurate than assuming that the surface is perfectly saturated or that the entire sea surface has a uniform saturation rate. Increasing the number of tracer observations in high latitudes in both winter and summer could help constrain the boundary conditions in the future. We do not account for the small lag in atmospheric CFC concentration between the northern and southern hemispheres which introduces a $\sim$6 month offset in waters of southern origin. In addition, a number of SF_6 tracer release experiments have introduced an artificial (i.e., non-atmospheric) source into the interior ocean over the last three decades. We assume this is a relatively small source of SF_6 in the ocean and note the ratio of CFCs to SF_6 would not be the same as the atmospheric history.

The oceanic histories of CFCs and SF_6 are less than a century old and thus their distributions likely still reflect fast pathways that result from advective transport. As advective pathways induce a tracer transport that is primarily isopycnal, it is a good assumption that the boundary condition, $C_{atm}(t)$ in Equation 1, is given by following the isopycnal surface of any interior point back to the surface. In regions such as the deep Pacific, diapycnal transport can no longer be assumed to be small, and it is no longer clear which value for $C_{atm}(t)$ is best. For the deep Pacific, in particular, ventilation occurs by horizontal advection of abyssal waters followed by slow upward diapycnal transport, and thus the most appropriate boundary condition may come from a denser density surface. Fortunately for this analysis of CFCs and SF_6, there is little penetration into the deep Pacific at this time.

At some point in the future, analyses of CFCs and SF_6 will have to take into account the effect of diapycnal transport for the inference of proper boundary conditions. Other tracers that have a longer history of variability, such as anthropogenic carbon, may already require such accounting. Methods that simultaneously invert tracer data for water-mass mixing and aging (DeVries & Primeau, 2011; Gebbie & Huybers, 2012) are a natural way to solve this problem, at the cost of requiring a global inversion with commensurate computational costs.

Here, we have demonstrated the ability to use tracers to evaluate variability in ocean ventilation and asses advection timescales in the deep ocean. In addition, our Green's

Functions can be convolved with any surface boundary conditions to assess ocean uptake of other quantities, including anthropogenic carbon and heat. Continuing to measure transit tracers through international programs such as GO-SHIP will be a key tool for assessing the uptake of anthropogenic heat and carbon by the ocean and monitoring variability in ocean ventilation and circulation.

6 Open Research

Data used here is publicly available from GLODAP (https://www.glodap.info/). AnSlope tracer data will be made available before publication via the CCHDO database.

Acknowledgments

We would like to thank all those who participated in the collection and curation of the thousands of CFCs and SF_6 bottles sampled and analysed through the international GO-SHIP and WOCE programs. This work was supported by NSF Award 1850772, NSF Award OCE-1850753, and the U.S. GO-SHIP NSF award 2023545.

References

Azetsu-Scott, K., Jones, E. P., Yashayaev, I., & Gershey, R. M. (2003). Time series study of cfc concentrations in the labrador sea during deep and shallow convection regimes (1991–2000). *Journal of Geophysical Research: Oceans*, *108*(C11).

Bullister, J., & Weiss, R. (1983). Anthropogenic chlorofluoromethanes in the greenland and norwegian seas. *Science*, *221*(4607), 265–268.

Bullister, J. L. (2015). Atmospheric histories (1765-2015) for cfc-11, cfc-12, cfc-113, ccl4, sf6 and n2o. *Carbon Dioxide Information Analysis Center, Oak Ridge National Laboratory, US Department of Energy, Oak Ridge, Tennessee*.

Bullister, J. L., Wisegarver, D., & Menzia, F. A. (2002). The solubility of sulfur hexafluoride in water and seawater. *Deep Sea Research Part I: Oceanographic Research Papers*, *49*(1), 175–187.

Cessi, P. (2019). The global overturning circulation. *Annual review of marine science*, *11*, 249–270.

DeVries, T., & Primeau, F. (2010). An improved method for estimating water-mass ventilation age from radiocarbon data. *Earth and Planetary Science Letters*, *295*(3-4), 367–378.

DeVries, T., & Primeau, F. (2011). Dynamically and observationally constrained estimates of water-mass distributions and ages in the global ocean. *Journal of Physical Oceanography*, *41*(12), 2381–2401.

Doney, S. C., & Bullister, J. L. (1992). A chlorofluorocarbon section in the eastern north atlantic. *Deep Sea Research Part A. Oceanographic Research Papers*, *39*(11-12), 1857–1883.

Fine, R. A. (2011). Observations of CFCs and SF6 as ocean tracers. *Annual Review of Marine Science*, *3*, 173–195.

Fine, R. A., Peacock, S., Maltrud, M. E., & Bryan, F. O. (2017). A new look at ocean ventilation time scales and their uncertainties. *Journal of Geophysical Research: Oceans*, *122*(5), 3771–3798.

Friedrichs, M. A., McCartney, M. S., & Hall, M. M. (1994). Hemispheric asymmetry of deep water transport modes in the western atlantic. *Journal of Geophysical Research: Oceans*, *99*(C12), 25165–25179.

Gebbie, G., & Huybers, P. (2010). Total matrix intercomparison: A method for determining the geometry of water-mass pathways. *Journal of Physical Oceanography*, *40*(8), 1710–1728.

Gebbie, G., & Huybers, P. (2012). The mean age of ocean waters inferred from radiocarbon observations: Sensitivity to surface sources and accounting for mixing histories. *Journal of Physical Oceanography*, *42*(2), 291–305.

Gordon, A. L. (2019). Bottom water formation. In J. K. Cochran, H. J. Bokuniewicz, & P. L. Yager (Eds.), *Encyclopedia of ocean sciences (third edition)* (Third Edition ed., p. 120-126). Oxford: Academic Press. Retrieved from `https://www.sciencedirect.com/science/article/pii/B9780124095489040197` doi: https://doi.org/10.1016/B978-0-12-409548-9.04019-7

Gordon, A. L., Orsi, A. H., Muench, R., Huber, B. A., Zambianchi, E., & Visbeck, M. (2009). Western ross sea continental slope gravity currents. *Deep Sea Research Part II: Topical Studies in Oceanography*, *56*(13-14), 796–817.

Gouretski, V., & Koltermann, K. P. (2004). Woce global hydrographic climatology. *Berichte des BSH*, *35*, 1–52.

Hall, T. M., Haine, T. W., & Waugh, D. W. (2002). Inferring the concentration of anthropogenic carbon in the ocean from tracers. *Global Biogeochemical Cycles*, *16*(4), 78–1.

Hall, T. M., Haine, T. W., Waugh, D. W., Holzer, M., Terenzi, F., & LeBel, D. A. (2007). Ventilation rates estimated from tracers in the presence of mixing. *Journal of physical oceanography*, *37*(11), 2599–2611.

Hall, T. M., Waugh, D. W., Haine, T. W., Robbins, P. E., & Khatiwala, S. (2004). Estimates of anthropogenic carbon in the indian ocean with allowance for mixing and time-varying air-sea co2 disequilibrium. *Global Biogeochemical Cycles*, *18*(1).

Herrford, J., Brandt, P., & Zenk, W. (2017). Property changes of deep and bottom waters in the western tropical atlantic. *Deep Sea Research Part I: Oceanographic Research Papers*, *124*, 103–125.

Holte, J., Talley, L. D., Gilson, J., & Roemmich, D. (2017). An argo mixed layer climatology and database. *Geophysical Research Letters*, *44*(11), 5618–5626.

Holzer, M., Primeau, F. W., Smethie Jr, W. M., & Khatiwala, S. (2010). Where and how long ago was water in the western north atlantic ventilated? maximum entropy inversions of bottle data from woce line a20. *Journal of Geophysical Research: Oceans*, *115*(C7).

Hood, E., Sabine, C., & Sloyan, B. (2010). The GO-SHIP repeat hydrography manual: A collection of expert reports and guidelines. *IOCCP Report Number 14, ICPO Publication Series Number 134.*. (Available online at http://www.go-ship.org/HydroMan.html)

Huhn, O., Rhein, M., Hoppema, M., & van Heuven, S. (2013). Decline of deep and bottom water ventilation and slowing down of anthropogenic carbon storage in the weddell sea, 1984–2011. *Deep Sea Research Part I: Oceanographic Research Papers*, *76*, 66–84.

Jackett, D., & McDougall, T. (1997). A neutral density variable for the world's oceans. *Journal of Physical Oceanography*, *27*, 237-263.

Jacobs, S. S., Fairbanks, R. G., & Horibe, Y. (1985). Origin and evolution of water masses near the antarctic continental margin: Evidence from h218o/h216o ratios in seawater. *Oceanology of the Antarctic continental shelf*, *43*, 59–85.

Johnson, G. C. (2008). Quantifying antarctic bottom water and north atlantic deep water volumes. *Journal of Geophysical Research: Oceans*, *113*(C5).

Johnson, H. L., Cessi, P., Marshall, D. P., Schloesser, F., & Spall, M. A. (2019). Recent contributions of theory to our understanding of the Atlantic Meridional Overturning Circulation. *Journal of Geophysical Research: Oceans*, *124*(8), 5376–5399.

Key, R., Tanhua, T., Olsen, A., Hoppema, M., Jutterström, S., Schirnick, C., ... others (2010). The carina data synthesis project: introduction and overview. *Earth System Science Data*, *2*(1), 105–121.

Khatiwala, S., Primeau, F., & Hall, T. (2009). Reconstruction of the history of anthropogenic co 2 concentrations in the ocean. *Nature*, *462*(7271), 346–349.

Khatiwala, S., Primeau, F., & Holzer, M. (2012). Ventilation of the deep ocean constrained with tracer observations and implications for radiocarbon estimates of ideal mean age. *Earth and Planetary Science Letters*, *325-326*, 116-125.

Koltermann, K. P., Gouretski, V., & Jancke, K. (2011). *Hydrographic atlas of the world ocean circulation experiment (WOCE). Volume 3: Atlantic Ocean.* National Oceanography Centre.

Lauvset, S. K., Lange, N., Tanhua, T., Bittig, H. C., Olsen, A., Kozyr, A., ... others (2021). An updated version of the global interior ocean biogeochemical data product, glodapv2. 2021. *Earth System Science Data*, *13*(12), 5565–5589.

LeBel, D. A., Smethie Jr, W. M., Rhein, M., Kieke, D., Fine, R. A., Bullister, J. L., ... others (2008). The formation rate of north atlantic deep water and eighteen degree water calculated from cfc-11 inventories observed during woce. *Deep Sea Research Part I: Oceanographic Research Papers*, *55*(8), 891–910.

Lozier, S. M. (1997). Evidence for large-scale eddy-driven gyres in the North Atlantic. *Science*, *277*(5324), 361–364.

Lozier, S. M., Bower, A., Furey, H., Drouin, K., Xu, X., & Zou, S. (2022). *Overflow water pathways in the north atlantic: New observations from the osnap program* (Tech. Rep.). Copernicus Meetings.

Lumpkin, R., & Speer, K. (2007). Global ocean meridional overturning. *Journal of Physical Oceanography.*, *37*, 2550-2562.

Mahieu, L., Lo Monaco, C., Metzl, N., Fin, J., & Mignon, C. (2020). Variability and stability of anthropogenic co 2 in antarctic bottom water observed in the indian sector of the southern ocean, 1978–2018. *Ocean Science*, *16*(6), 1559–1576.

Maiss, M., & Brenninkmeijer, C. A. (1998). Atmospheric sf6: trends, sources, and prospects. *Environmental Science & Technology*, *32*(20), 3077–3086.

Matear, R., & McNeil, B. (2003). Decadal accumulation of anthropogenic co2 in the southern ocean: A comparison of cfc-age derived estimates to multiple-linear regression estimates. *Global Biogeochemical Cycles*, *17*(4).

Morrison, A. K., Waugh, D. W., Hogg, A. M., Jones, D. C., & Abernathey, R. P. (2022). Ventilation of the southern ocean pycnocline. *Annual Review of Marine Science*, *14*, 405–430.

Murata, A., Kumamoto, Y.-i., & Sasaki, K.-i. (2019). Decadal-scale increases of anthropogenic co2 in antarctic bottom water in the indian and western pacific sectors of the southern ocean. *Geophysical Research Letters*, *46*(2), 833–841.

Orsi, A. H., Jacobs, S. S., Gordon, A. L., & Visbeck, M. (2001). Cooling and ventilating the abyssal ocean. *Geophysical Research Letters*, *28*(15), 2923–2926.

Orsi, A. H., Johnson, G. C., & Bullister, J. L. (1999). Circulation, mixing, and production of Antarctic Bottom Water. *Progress in Oceanography*, *43*(1), 55–109.

Orsi, A. H., Smethie Jr, W. M., & Bullister, J. L. (2002). On the total input of antarctic waters to the deep ocean: A preliminary estimate from chlorofluorocarbon measurements. *Journal of Geophysical Research: Oceans*, *107*(C8), 31–1.

Prinn, R., Weiss, R., Fraser, P., Simmonds, P., Cunnold, D., Alyea, F., ... others (2000). A history of chemically and radiatively important gases in air deduced from ale/gage/agage. *Journal of Geophysical Research: Atmospheres*, *105*(D14), 17751–17792.

Purkey, S. G., Smethie Jr, W. M., Gebbie, G., Gordon, A. L., Sonnerup, R. E., Warner, M. J., & Bullister, J. L. (2018). A synoptic view of the ventilation and circulation of antarctic bottom water from chlorofluorocarbons and natural tracers. *Annual review of marine science*, *10*, 503–527.

Reid, J. L. (1994). On the total geostrophic circulation of the North Atlantic ocean: Flow patterns, tracers, and transports. *Progress in Oceanography*, *33*(1),

1–92.

Reid, J. L. (1997). On the total geostrophic circulation of the pacific ocean: Flow patterns, tracers, and transports. *Progress in Oceanography*, *39*(4), 263–352.

Reid, J. L. (2003). On the total geostrophic circulation of the indian ocean: Flow patterns, tracers, and transports. *Progress in Oceanography*, *56*(1), 137–186.

Rhein, M. (1994). The deep western boundary current: tracers and velocities. *Deep Sea Research Part I: Oceanographic Research Papers*, *41*(2), 263–281.

Rhein, M., Kieke, D., & Steinfeldt, R. (2015). Advection of n orth a tlantic d eep w ater from the l abrador s ea to the southern hemisphere. *Journal of Geophysical Research: Oceans*, *120*(4), 2471–2487.

Rhein, M., Stramma, L., & Send, U. (1995). The atlantic deep western boundary current: Water masses and transports near the equator. *Journal of Geophysical Research: Oceans*, *100*(C2), 2441–2457.

Rhein, M., Walter, M., Mertens, C., Steinfeldt, R., & Kieke, D. (2004). The circulation of north atlantic deep water at 16 n, 2000–2003. *Geophysical Research Letters*, *31*(14).

Ríos, A. F., Velo, A., Pardo, P. C., Hoppema, M., & Pérez, F. F. (2012). An update of anthropogenic co2 storage rates in the western south atlantic basin and the role of antarctic bottom water. *Journal of Marine Systems*, *94*, 197–203.

Rivaro, P., Ianni, C., Magi, E., Massolo, S., Budillon, G., & Smethie Jr, W. M. (2015). Distribution and ventilation of water masses in the western ross sea inferred from cfc measurements. *Deep Sea Research Part I: Oceanographic Research Papers*, *97*, 19–28.

Rodehacke, C. B., Roether, W., Hellmer, H. H., & Hall, T. (2010). Temporal variations and trends of CFC11 and CFC12 surface-water saturations in Antarctic marginal seas: Results of a regional ocean circulation model. *Deep. Res. Part I Oceanogr. Res. Pap.*, *57*(2), 175–198.

Roemmich, D. (1983). Optimal estimation of hydrographic station data and derived fields. *Journal of Physical Oceanography*, *13*(8), 1544–1549.

Rosell-Fieschi, M., Pelegrí, J. L., & Gourrion, J. (2015). Zonal jets in the equatorial atlantic ocean. *Progress in Oceanography*, *130*, 1–18.

Sarmiento, J. L., & Sundquist, E. (1992). Revised budget for the oceanic uptake of anthropogenic carbon dioxide. *Nature*, *356*(6370), 589–593.

Schott, F. A., Dengler, M., Brandt, P., Affler, K., Fischer, J., Bourles, B., ... Rhein, M. (2003). The zonal currents and transports at 35 w in the tropical atlantic. *Geophysical Research Letters*, *30*(7).

Shao, A. E., Mecking, S., Thompson, L., & Sonnerup, R. E. (2013). Mixed layer saturations of cfc-11, cfc-12, and sf6 in a global isopycnal model. *Journal of Geophysical Research: Oceans*, *118*(10), 4978–4988.

Smeed, D., McCarthy, G., Cunningham, S., Frajka-Williams, E., Rayner, D., Johns, W., ... Bryden, H. (2014). Observed decline of the Atlantic meridional overturning circulation 2004-2012. *Ocean Science*, *10*(1), 29–38.

Smethie, W. M., Fine, R. A., Putzka, A., & Jones, E. P. (2000). Tracing the flow of north atlantic deep water using chlorofluorocarbons. *Journal of Geophysical Research: Oceans*, *105*(C6), 14297–14323.

Smethie Jr, W. M. (1993). Tracing the thermohaline circulation in the western north atlantic using chlorofluorocarbons. *Progress in Oceanography*, *31*(1), 51–99.

Smethie Jr, W. M., & Fine, R. A. (2001). Rates of north atlantic deep water formation calculated from chlorofluorocarbon inventories. *Deep Sea Research Part I: Oceanographic Research Papers*, *48*(1), 189–215.

Smethie Jr, W. M., & Jacobs, S. S. (2005). Circulation and melting under the ross ice shelf: estimates from evolving cfc, salinity and temperature fields in the ross sea. *Deep Sea Research Part I: Oceanographic Research Papers*, *52*(6), 959–978.

Solodoch, A., Stewart, A., Hogg, A. M., Morrison, A., Kiss, A., Thompson, A., ...

Cimoli, L. (2022). How does antarctic bottom water cross the southern ocean? *Geophysical Research Letters*, *49*(7), e2021GL097211.

Stöven, T., Tanhua, T., Hoppema, M., & Bullister, J. (2015). Perspectives of transient tracer applications and limiting cases. *Ocean Science*, *11*, 699–718.

Talley, L. D. (2008). Freshwater transport estimates and the global overturning circulation: Shallow, deep and throughflow components. *Progress in Oceanography*, *78*(4), 257–303.

Talley, L. D., Reid, J. L., & Robbins, P. E. (2003). Data-based meridional overturning streamfunctions for the global ocean. *Journal of Climate*, *16*(19), 3213–3226.

Tanhua, T., Jones, E. P., Jeansson, E., Jutterström, S., Smethie Jr, W. M., Wallace, D. W., & Anderson, L. G. (2009). Ventilation of the arctic ocean: Mean ages and inventories of anthropogenic co2 and cfc-11. *Journal of Geophysical Research: Oceans*, *114*(C1).

Tanhua, T., Waugh, D. W., & Bullister, J. L. (2013). Estimating changes in ocean ventilation from early 1990s cfc-12 and late 2000s sf6 measurements. *Geophysical Research Letters*, *40*(5), 927–932.

Ting, Y.-H., & Holzer, M. (2017). Decadal changes in southern ocean ventilation inferred from deconvolutions of repeat hydrographies. *Geophysical Research Letters*, *44*(11), 5655–5664.

Trossman, D., Thompson, L., Mecking, S., Warner, M., Bryan, F., & Peacock, S. (2014). Evaluation of oceanic transport parameters using transient tracers from observations and model output. *Ocean Modelling*, *74*, 1–21.

Walker, S. J., Weiss, R. F., & Salameh, P. K. (2000). Reconstructed histories of the annual mean atmospheric mole fractions for the halocarbons cfc-11 cfc-12, cfc-113, and carbon tetrachloride. *Journal of Geophysical Research: Oceans*, *105*(C6), 14285–14296.

Warner, M. J., & Weiss, R. F. (1985). Solubilities of chlorofluorocarbons 11 and 12 in water and seawater. *Deep Sea Research Part A. Oceanographic Research Papers*, *32*(12), 1485–1497.

Waugh, D. W., Haine, T. W., & Hall, T. M. (2004). Transport times and anthropogenic carbon in the subpolar north atlantic ocean. *Deep Sea Research Part I: Oceanographic Research Papers*, *51*(11), 1475–1491.

Waugh, D. W., Hall, T. M., & Haine, T. W. (2003). Relationships among tracer ages. *Journal of Geophysical Research: Oceans*, *108*(C5).

Waugh, D. W., Primeau, F., DeVries, T., & Holzer, M. (2013). Recent changes in the ventilation of the southern oceans. *science*, *339*(6119), 568–570.

Weiss, R. F., Bullister, J. L., Gammon, R. H., & Warner, M. J. (1985). Atmospheric chlorofluoromethanes in the deep equatorial atlantic. *Nature*, *314*(6012), 608–610.

Willey, D. A., Fine, R. A., Sonnerup, R. E., Bullister, J. L., Smethie Jr, W. M., & Warner, M. J. (2004). Global oceanic chlorofluorocarbon inventory. *Geophysical Research Letters*, *31*(1).

Supporting Information for "Annually-resolved propagation of CFCs and SF_6 over eight decades"

Laura Cimoli[1], Geoffrey Gebbie[2], Sarah G. Purkey[1], William M. Smethie[3]

[1]Scripps Institution of Oceanography, University of California, San Diego

[2]Woods Hole Oceanographic Institution, Woods Hole, Massachusetts

[3]Lamont-Doherty Earth Observatory, Columbia University

Contents of this file

1. Text S1
2. Figures S1 to S5

Introduction

The supplementary information in Text S1 reports the details of how to construct and solve the modified, non-negative least squares problem to deconvolve the discrete Green's function **G** (together with the information reported in Section 3.2 of the main manuscript).

Supplementary Figures S1 and S2 also provide additional details about the Time-Correction Method, in particular about the decisions made in this study to calculate the surface boundary conditions (Figure S1) and the first guess Green's function (Figure S2).

Figures S3 and S4 report the reconstructed CFC-12 and SF_6 concentrations in 2021 for the hydrographic sections A16-A23, P16 and I8I9. The reconstructed CFC-11 concentrations are shown in the main manuscript (Figure 4).

Figure S5 shows the vertically-integrated CFC-11 concentration reconstructed with the TCM in 1994 and 2020. The 1994 year was chosen for a direct comparison to the CFC-11 inventory by Willey et al. (2004). Note that our product is not gridded on a uniform horizontal and vertical grid, such as the CFC-11 inventory by Willey et al. (2004); as such, in the vertical integration of the reconstructed CFC-11 we examine only the locations where observations describe at least 66% of the water column. This choice explains the lack of data in the southwest Indian Ocean, in the Atlantic sector of the Southern Ocean and partially in the east Pacific Ocean.

Text S1. To solve the least squares problem to find $\mathbf{G}$, at each location we define:

$$\hat{\mathbf{C}} = \begin{bmatrix} \mathbf{C}_1 \\ \hline \mathbf{C}_2 \\ \hline \vdots \\ \hline \mathbf{C}_{N_t} \\ \hline \mathbf{G}_0 \end{bmatrix}, \; \hat{C}_s = \begin{bmatrix} C_{s1} \\ \hline C_{s2} \\ \hline \vdots \\ \hline C_{sN_t} \\ \hline \mathbf{I} \end{bmatrix}, \; \hat{W}^{-1} = \begin{bmatrix} W_1^{-1} & 0 & 0 & 0 & 0 \\ \hline 0 & W_2^{-1} & 0 & 0 & 0 \\ \hline 0 & 0 & \ddots & 0 & \\ \hline 0 & 0 & 0 & W_{N_t}^{-1} & 0 \\ \hline 0 & 0 & 0 & 0 & S^{-1} \end{bmatrix}.$$

N_t is the number of tracers used (depending on the available observations), and $\mathbf{C}_i$ represents the array of observations available at one location in the ocean interior for each tracer. The C_{si} matrix returns the surface boundary conditions per each tracer, while W_i^{-1} and S^{-1} indicate the weight matrices for the tracer observations and the Green's function first guess $\mathbf{G}_0$, respectively. We re-arrange the terms reported above to use the non-negative least-squares method of Lawson and Hanson (1995), defining

$$\begin{aligned} \hat{\hat{\mathbf{C}}} &= \hat{W}^{-1/2}\hat{\mathbf{C}} \\ \hat{\hat{\mathbf{C}}}_s &= \hat{W}^{-1/2}\hat{\mathbf{C}}_s \end{aligned} \tag{1}$$

which we can use to rewrite the cost function as

$$J = (\hat{\hat{\mathbf{C}}} - \hat{\hat{C}}_s\mathbf{G})^T(\hat{\hat{\mathbf{C}}} - \hat{\hat{C}}_s\mathbf{G}), \tag{2}$$

which is equivalent to solving the equation $\hat{\hat{C}}_s\mathbf{G} = \hat{\hat{\mathbf{C}}}$, going back to the canonical form of a least-squares problem.

References

Holte, J., Talley, L. D., Gilson, J., & Roemmich, D. (2017). An argo mixed layer climatology and database. *Geophysical Research Letters*, *44*(11), 5618–5626.

Lawson, C. L., & Hanson, R. J. (1995). *Solving least squares problems*. SIAM.

Willey, D. A., Fine, R. A., Sonnerup, R. E., Bullister, J. L., Smethie Jr, W. M., & Warner, M. J. (2004). Global oceanic chlorofluorocarbon inventory. *Geophysical Research Letters*, *31*(1).

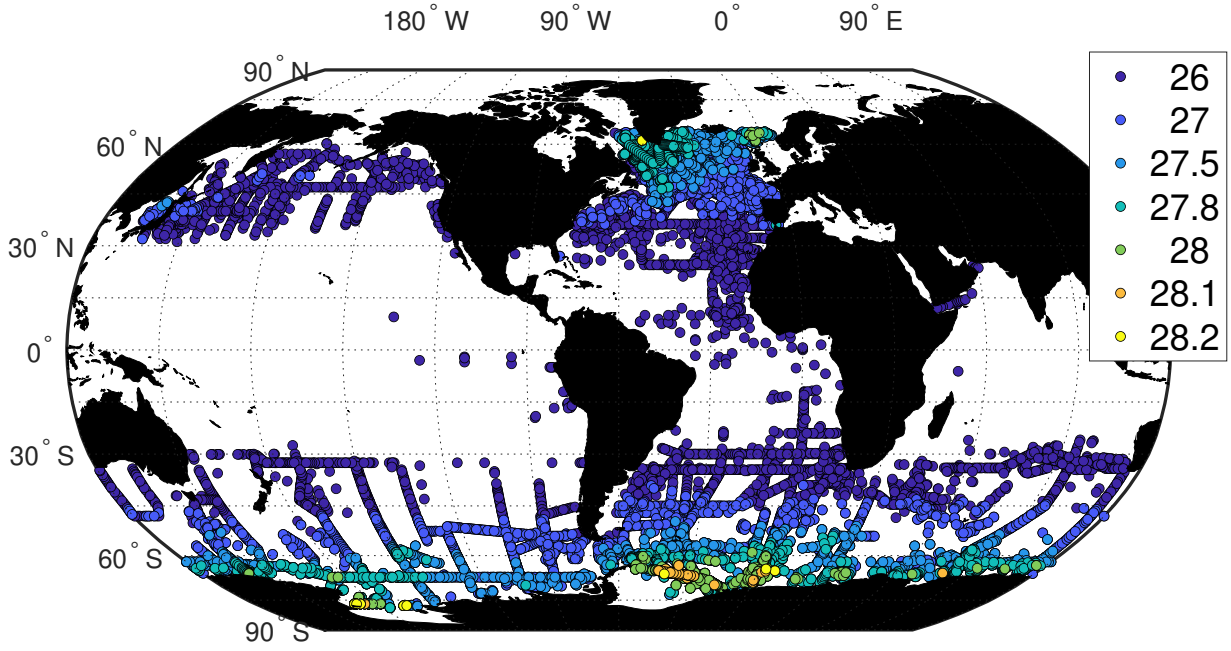

Figure S1. Outcrop points for the neutral density levels indicated in the legend. Outcrop points are defined as locations where the maximum mixed layer depth (from Holte et al. (2017)) is found at a density larger than a specific density level.

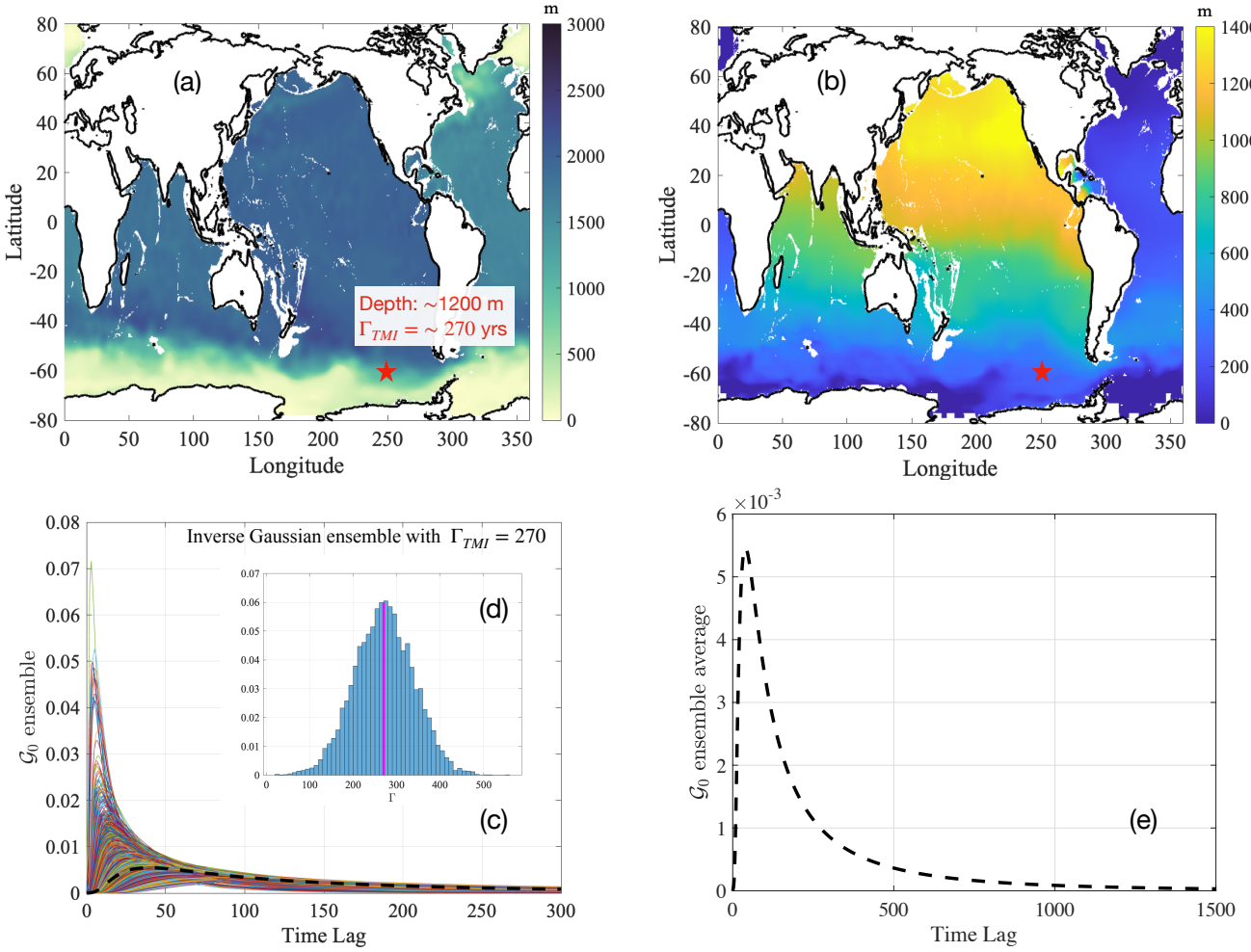

Figure S2. Steps to define the first guess $\mathbf{G}_0$: example at 150°W, 60°S on neutral density surface $\gamma^n = 27.90$ (red star in panels a, b). For each location, we find the closest TMI water age estimate. (a)-(b) Depth and Γ_{TMI} of the density surface. At the starred location, $\gamma^n = 27.90$ is about 1200 m deep and the TMI water age estimate is $\Gamma_{TMI} = 270$ years. (c) Ensemble of Inverse Gaussians with age within the range $\Gamma_{TMI}/2 : \Gamma_{TMI}$ x2 (see subset histogram in panel (d)). The ensemble average returns the kernel first guess used here, $\mathbf{G}_0$ (indicated in panel d, and shown in panel e).

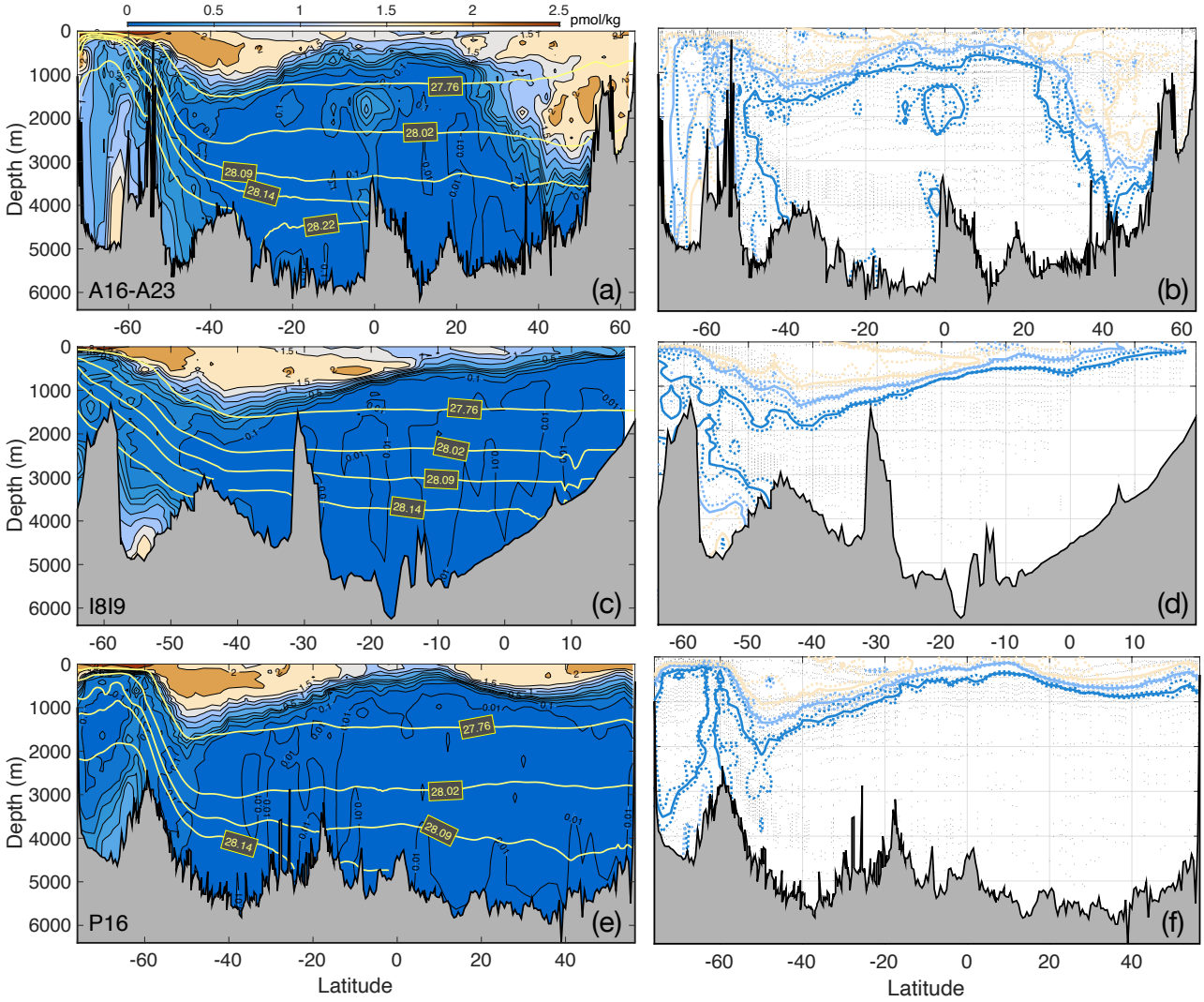

Figure S3. Reconstructed CFC-12 concentrations along A16+A23 (panels a,b), I8I9 (c,d), and P16 (e,f) in 2021. Panels in left column show the reconstructed concentration and neutral density contours (yellow) along each section. Panels in right column show the observation locations throughout all decades of available data (gray dots) and the uncertainty of the time corrected CFC-12 concentrations for three contours (0.2, 0.75 and 1.5 pmol/kg). The solid line shows our best estimate, while the dotted lines show the 95% confidence limits.

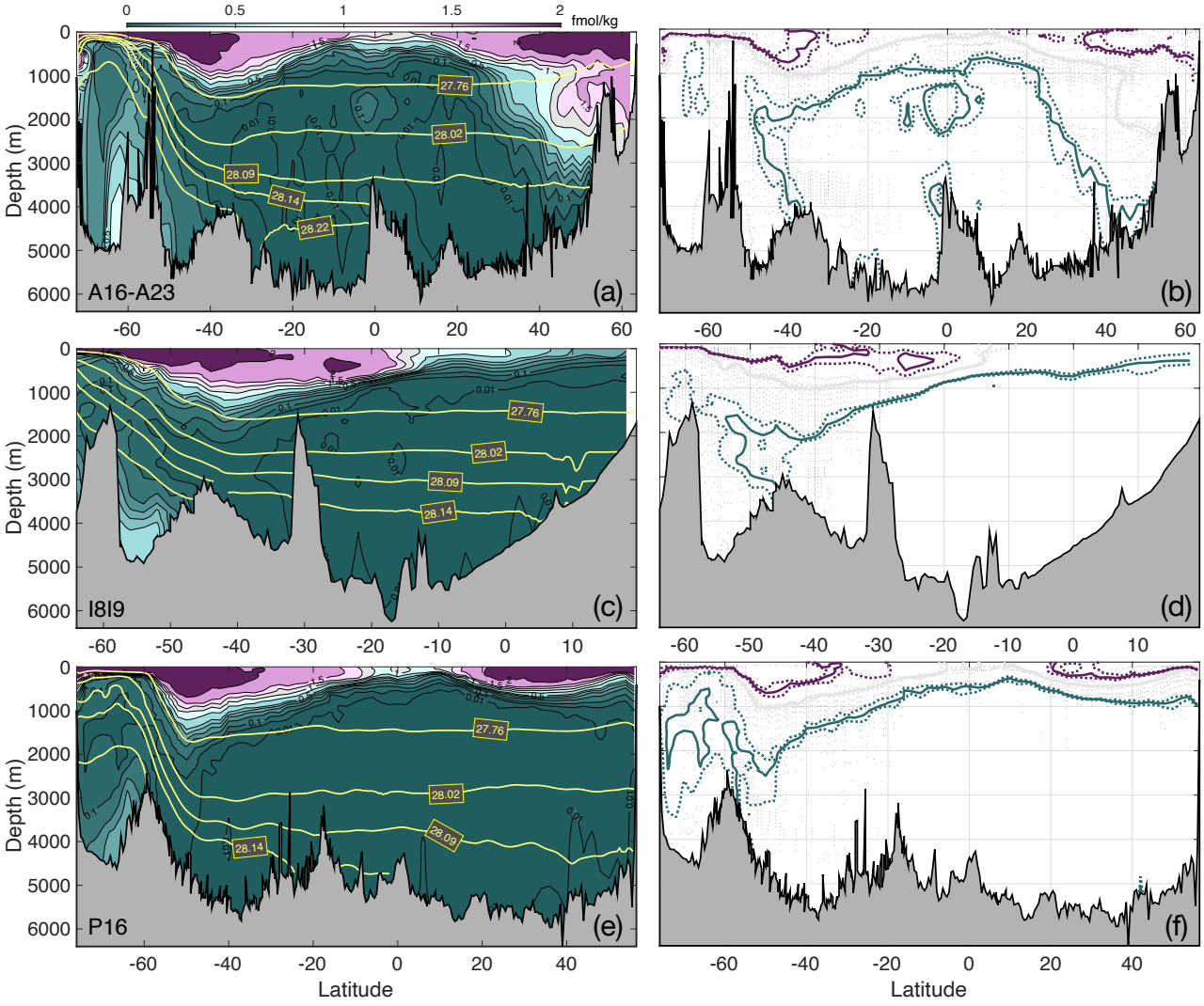

Figure S4. Same as in Figure S3 but for SF_6. The uncertainty of the time corrected SF_6 concentrations is shown for the contours 0.05, 1 and 2 fmol/kg.

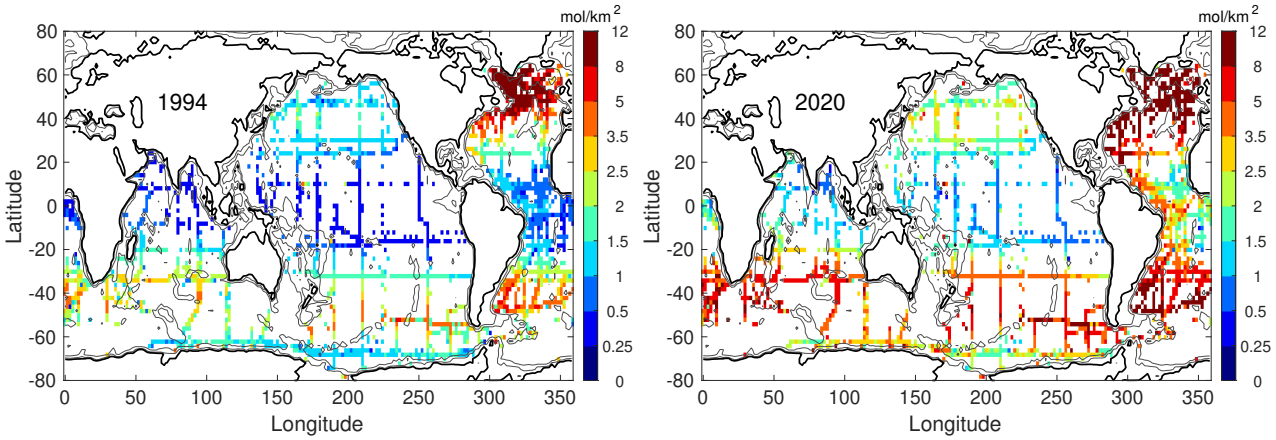

Figure S5. Vertically-integrated CFC-11 concentrations in 1994 (which can be compared with the inventory presented in Willey et al. (2004)) and 2020.